Title: Top-down control of flight by a non-canonical cortico-amygdala pathway

Authors: Chandrashekhar D. Borkar[1,2], Claire E. Stelly[1,2], Xin Fu[2,3], Maria Dorofeikova[1,2], Quan-Son Eric Le[2,3], Rithvik Vutukuri[2,3], Catherine Vo[2,3], Alex Walker[2,3], Samhita Basavanhalli[2,3], Anh Duong[2,3], Erin Bean[2,3], Alexis Resendez[1,2], Jones G. Parker[4], Jeffrey G. Tasker[2,5], Jonathan P. Fadok[1,2]*

Affiliations:

[1] Department of Psychology, Tulane University, New Orleans, LA 70118, USA

[2] Tulane Brain Institute, Tulane University, New Orleans, LA 70118, USA

[3] Neuroscience Program, Tulane University, New Orleans, LA 70118, USA

[4] Department of Neuroscience, Feinberg School of Medicine, Northwestern University, Chicago, IL 60611, USA

[5] Department of Cell and Molecular Biology, Tulane University, New Orleans, LA 70118, USA

*Corresponding author: Jonathan P. Fadok

Tulane Brain Institute, 6823 St. Charles Ave., New Orleans, LA 70118-5698, USA.

E-mail address: jfadok@tulane.edu.

Survival requires the selection of appropriate behaviour in response to threats, and dysregulated defensive reactions are associated with psychiatric illnesses such as posttraumatic stress and panic disorder.[1] Threat-induced behaviours, including freezing and flight, are controlled by neuronal circuits in the central amygdala (CeA)[2]; however, the source of neuronal excitation to the CeA that contributes to high-intensity defensive responses is unknown. Here we used a combination of neuroanatomical mapping, *in-vivo* calcium imaging, functional manipulations, and electrophysiology to characterize a previously unknown projection from the dorsal peduncular (DP) prefrontal cortex to the

CeA. DP-to-CeA neurons are glutamatergic and specifically target the medial CeA, the main amygdalar output nucleus. Using a behavioural paradigm that elicits both freezing and flight, we found that CeA-projecting DP neurons are activated by high-intensity threats in a context-dependent manner. Functional manipulations revealed that the DP-to-CeA pathway is necessary and sufficient for both avoidance behaviour and flight. Furthermore, we found that DP projections target distinct medial CeA neuronal populations projecting to midbrain flight centres. These results elucidate a non-canonical top-down pathway regulating defensive responses.

In the face of threat, organisms display a continuum of defensive behaviours and flexibly shift between defensive strategies.[3,4] Selecting the appropriate action for survival depends on the proximity and intensity of the threat and the context of the encounter.[5,6] Moreover, exaggerated responses to perceived threats have been associated with anxiety, post-traumatic stress and panic disorders, and phobias.[1,7,8,9] Abnormal patterns of activation in the prefrontal cortex (PFC) are associated with these mental illnesses, and bidirectional projections between the medial PFC (mPFC) and basolateral amygdala are part of a canonical pathway that has been extensively studied in the acquisition and expression of learned fear measured with freezing.[10–14] Previous studies have shown that animals exhibit behavioural scaling to favour flight over freezing in response to a high-intensity threat, and conditional freeze-to-flight shifting is regulated by distinct and mutually inhibitory local circuit motifs in the CeA.[2,15,16] Whether the cortex exerts top-down control of these behavioural shifts is not known. Interestingly, the mPFC also projects to the CeA,[17] raising the possibility that a direct pathway from mPFC to CeA could influence defensive action selection. However, this pathway has never been defined neuroanatomically, and its role in regulating defensive behaviour is unknown.

Direct mPFC projections to medial CeA

53 To determine which subdivision of the mPFC projects to the CeA, we injected fluorescent,
54 retrogradely trafficked latex microspheres into the CeA (**Fig. 1A, B**). We observed sparse
55 projections from both the prelimbic (PL) and infralimbic (IL) cortices. However, a significantly
56 greater number of CeA projectors were located in the dorsal peduncular nucleus (DP; **Fig. 1C, D;**
57 **Fig. S1A**), a region of the mPFC recently linked to physiological and behavioural responses to
58 stress.[18]
59
60 The mPFC regulates cognition, motivation, and emotion via distinct glutamatergic projections to
61 cortical and subcortical regions.[19] The vesicular glutamate transporter (Vglut) 1 is used to label
62 most excitatory cortical neurons, yet the DP is enriched in both the Vglut1 and Vglut2 isoforms,
63 which define different populations of projection neurons.[20] To characterize the DP-to-CeA
64 pathway more precisely, we injected a Cre-dependent mCherry vector into the DP of Vglut1- or
65 Vglut2-Cre mice and quantified fibre density in CeA subnuclei (**Fig. 1E–G**). We found that, while
66 the mCherry+ fibre density within the CeA was significantly higher in Vglut1 mice (**Fig. 1H–J**),
67 notably, in both Vglut1 and Vglut2 mice, mCherry+ fibres were most abundant in the medial
68 subdivision of the CeA (CeM), as compared to the lateral (CeL) or capsular (CeC) subdivisions
69 (**Fig. 1J**). Therefore, Vglut1- and 2-expressing DP neurons are anatomically positioned to
70 influence the function of the primary amygdalar output centre controlling the expression of
71 adaptive behaviour.

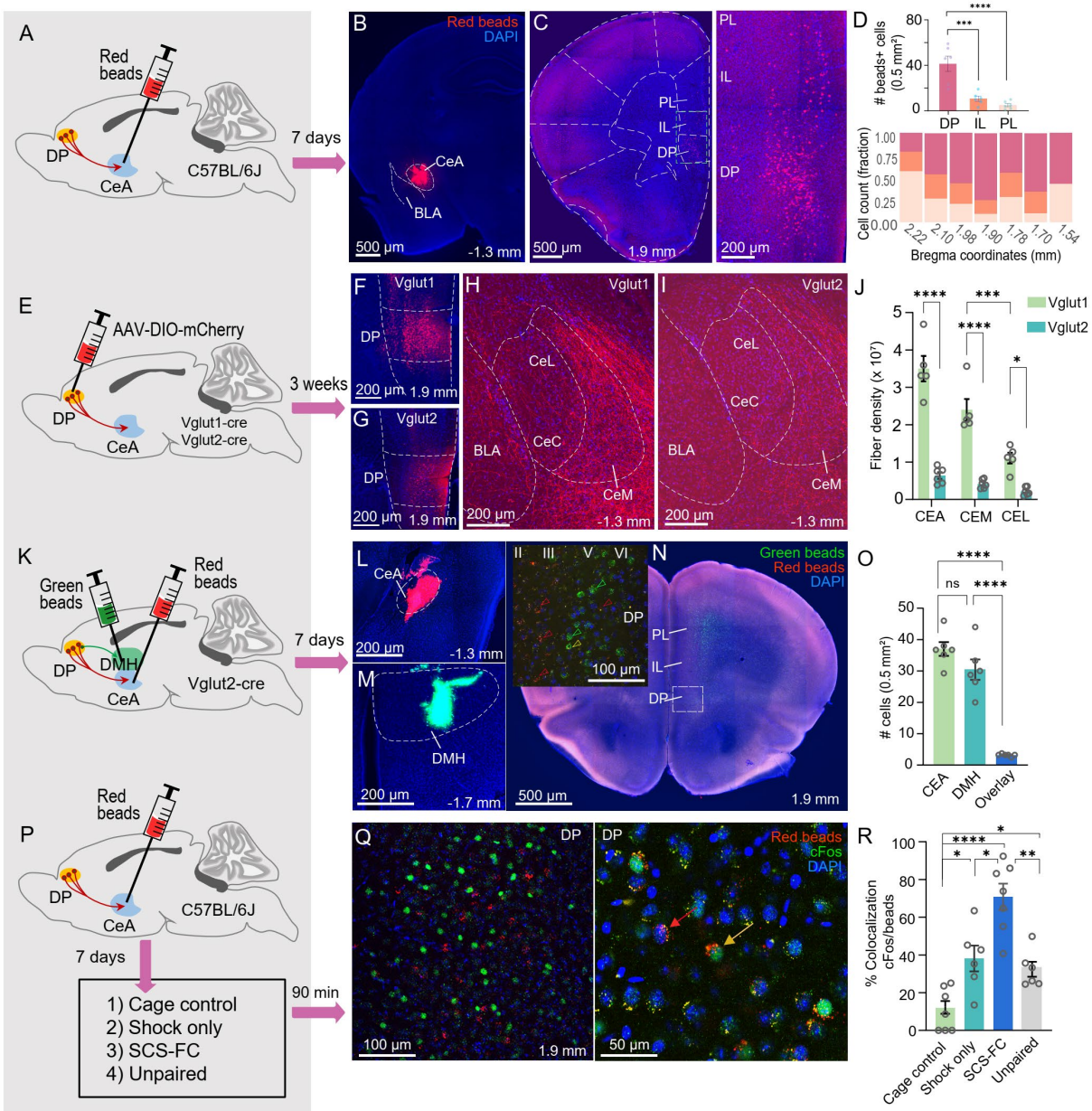

Figure 1. Neuroanatomical characterization of the DP-to-CeA pathway.

A, Schematic diagram showing retrograde tracing strategy.

B, Histology image showing injection site of red beads in the CeA.

C, Histology images of red retro-beads+ neurons in the DP (at 5x *(left)* and 10x *(right)* magnification).

D, *Top,* A significantly higher proportion of mPFC CeA-projecting neurons are in the DP, compared to the IL or PL (One-way ANOVA, $F_{(2,15)} = 21.86$, $p < 0.0001$; Bonferroni's post-hoc test, ***$p<0.001$, **** $p<0.0001$; N = 6). Data represented as means ± s.e.m. *Bottom*, Distribution of CeA-projecting neurons along the mPFC antero-posterior axis (N = 6; 4-6 sections/mouse). DP, dorsal peduncular cortex; IL, infralimbic cortex; PL, prelimbic cortex.

E, Strategy used to trace glutamatergic terminals in the CeA.

F, Representative image of DP targeting in Vglut1-Cre mice.

G, Representative image of DP targeting in Vglut2-Cre mice.

H, Representative expression of mCherry+ terminals in the CeA of a VGlut1-Cre mouse.

I, Representative expression of mCherry+ terminals in the CeA of a VGlut2-Cre mouse.

J, Integrated density of mCherry+ fibres from Vglut1+ (N = 5, 3-4 sections/mouse) and Vglut2+ (N = 6, 2-3 sections/mouse) neurons (unpaired Student's t-test for total CeA, Vglut1 vs Vglut2, t = 8.89, df = 9, $p < 0.0001$. Two-way ANOVA, CeM vs CeL, strain X region, $F_{(1,18)} = 12.6$, $p < 0.01$; Bonferroni's post-hoc test, *$p < 0.05$, ****$p < 0.0001$. CeL includes lateral and capsular subregions. Data represented as means ± s.e.m.

K, Dual-target retrograde tracing strategy from CeA and dorsomedial hypothalamus (DMH).

L, Representative targeting of CeA.

M, Representative targeting of DMH.

N, Deposition of green and red beads in the mPFC. *Inset,* distribution of CeA and DMH projectors in different layers of DP. Red, green, and yellow arrowheads indicate red beads, green beads, and overlay, respectively.

O, Number of DP neurons projecting to CeA, DMH, or both (One-way ANOVA, $F_{(2,15)} = 62.06$, $p = 0.0001$; Bonferroni's post-hoc test, ****$p < 0.0001$; N = 6, 3 sections/mouse). Data represented as means ± s.e.m.

102 **P**, Strategy for neuronal activation analysis. Seven days after injection, animals were split into
103 four groups: home cage control, shock only control, unpaired control, and serial compound
104 stimulus fear conditioning (SCS-FC).
105 **Q**, Representative images showing bead+ and/or cFos+ cells in the DP. *Left*, 10x and *Right*, 20x
106 magnifications. Red arrow, bead+; yellow arrow, bead and cFos+.
107 **R**, Quantification of cFos expression in bead+ cells (N = 6-7 mice; 3-4 sections/mouse; One-
108 way ANOVA, $F_{(3,22)} = 14.47$, $p < 0.0001$; Bonferroni's post-hoc test, *$p < 0.05$, **$p < 0.001$, ****p
109 < 0.0001). Data represented as means ± s.e.m.
110
111 The DP also projects to the dorsomedial hypothalamus (DMH), a pathway known to regulate
112 sympathetic responses to psychosocial stress.[18] To determine whether the DP-to-CeA and DP-
113 to-DMH pathways are discrete, we injected red or green-fluorescent retro-beads into the CeA and
114 DMH (**Fig. 1K–M**). Both red and green retro-beads were localized in DP cells (**Fig. 1N**), but the
115 DMH-projecting DP neurons were localized in layers V and VI (*90% vs 8.7%* in layer II/III),
116 whereas CeA-projecting cells were found mostly in layers II/III (**Fig. 1N, *inset;* Fig. S1B**, *87% vs*
117 *10.5%* in layers V and VI). Only a small number of DP cells (~7%) were co-labelled, suggesting
118 that the DP-to-CeA and DP-to-DMH pathways are anatomically distinct (**Fig. 1O; Fig. S1B**).
119
120 Given the role of the CeA in defensive response selection and the role of the DP in stress
121 responding,[2,18] we hypothesized that threats would activate CeA-projecting DP neurons. To test
122 this, we injected C57BL/6J mice with retro-beads in the CeA and divided animals into four groups:
123 home cage control, footshock-only, unpaired, and fear conditioning (**Fig. 1P**). The fear
124 conditioning (FC) group was subjected to a protocol we developed that elicits freezing and flight
125 responses to separate components of a serial compound stimulus (SCS-FC; **Fig. S1D–E**).[2]
126 Compared to home cage control, shock-only, and unpaired groups, SCS-FC mice displayed
127 significantly greater numbers of retro-bead+ cells in the DP that were co-labelled with cFos (**Fig.**

128 **1Q, R**). There were no significant differences in the total number of retro-bead+ cells across the
129 groups, indicating a consistent retrograde labelling efficiency across the experimental groups
130 (**Fig. S1C**).
131
132 **DP-to-CeA neurons are activated by flight**
133 The significantly elevated expression of cFos in the SCS-FC group suggests that DP-to-CeA
134 neurons are recruited most under conditions that elicit robust cue-induced defensive behaviour.
135 Therefore, we set out to determine the activation patterns of DP-to-CeA projecting neurons during
136 our SCS-FC protocol, which induces escalating intensities of defensive behaviours (**Fig. S1D, E**).
137 We used an intersectional approach to selectively express GCaMP6f in DP-to-CeA projection
138 neurons and imaged *in-vivo* calcium activity in freely moving mice using custom-built open-source
139 miniscopes (**Fig. 2A–C)**. We observed low levels of freezing and no flight before conditioning
140 (**Fig. S2A–D**), with similar levels of neuronal activation to the tone and white noise (WN)
141 components of the SCS (**Fig. S2E–J**). Moreover, there was no correlation between calcium
142 activity and movement speed before conditioning (**Fig. S2G**). Following conditioning, mice
143 exhibited elevated levels of freezing to the tone, and flight to the WN in the conditioning context
144 (hereafter called the high-threat context; **Fig. 2D–E; Fig. S3A–B**).[2,21] By contrast, mice exhibited
145 predominantly freezing when exposed to the same conditioned stimuli in a neutral context
146 (hereafter called the low-threat context; **Fig. 2M–N; Fig. S3I–J**). Interestingly, as conditioning
147 progressed, the mean activity of CeA-projecting DP neurons increased concurrently, which
148 correlated significantly with speed in the high- but not low-threat context (**Fig. S3C, K**).
149
150 In the high-threat context, the CeA-projecting DP neuronal population was most active during WN
151 and shock (**Fig. 2F–I**), with many individual DP-to-CeA neurons active specifically during sensory
152 epochs eliciting flight behaviour (WN and post-shock periods, 45% of recorded neurons; **Fig. 2G–**
153 **H; Fig. S3G–H**). Only 2% of cells encoded the tone (**Fig. 2H**) and average neuronal activity was

154 significantly higher during WN and post-shock compared to the tone (**Fig. 2I**). Interestingly, WN-
155 induced activation was diminished in the low-threat context (**Fig. 2O**), neuronal responses were
156 more evenly distributed across sensory epochs (**Fig. 2P–Q**), and no significant difference was
157 observed between neuronal responses to tone and WN (**Fig. 2R; Fig. S3O–P**). Together, these
158 data suggest that DP-to-CeA neuronal activity is context-dependent and is more associated with
159 sensory stimuli that induce higher-intensity threat behaviour.
160
161 To determine if DP-to-CEA projector activity is associated with defensive responses, we analysed
162 neuronal activity around the onset of freezing and flight bouts in both contexts. In the high-threat
163 context, neuronal activity was significantly increased at the onset of flight yet was unchanged in
164 response to freezing (**Fig. 2J–K)**. Neuronal activity was also positively correlated with speed,
165 during flight bouts (**Fig. 2L; Fig. S3D**), but not with locomotion surrounding freezing bouts (**Fig.**
166 **S3E–F**). Flight occasionally occurs in the low-threat context; therefore, we also analysed neuronal
167 responses to flight and freezing onset under these conditions. Just as in the high-threat context,
168 there was a significant increase in activity following flight onset, and a significant correlation
169 between neuronal activation and speed during flight, yet no increase in activity was noted for
170 freezing (**Fig. 2S–U; Fig. S3L–N**).
171

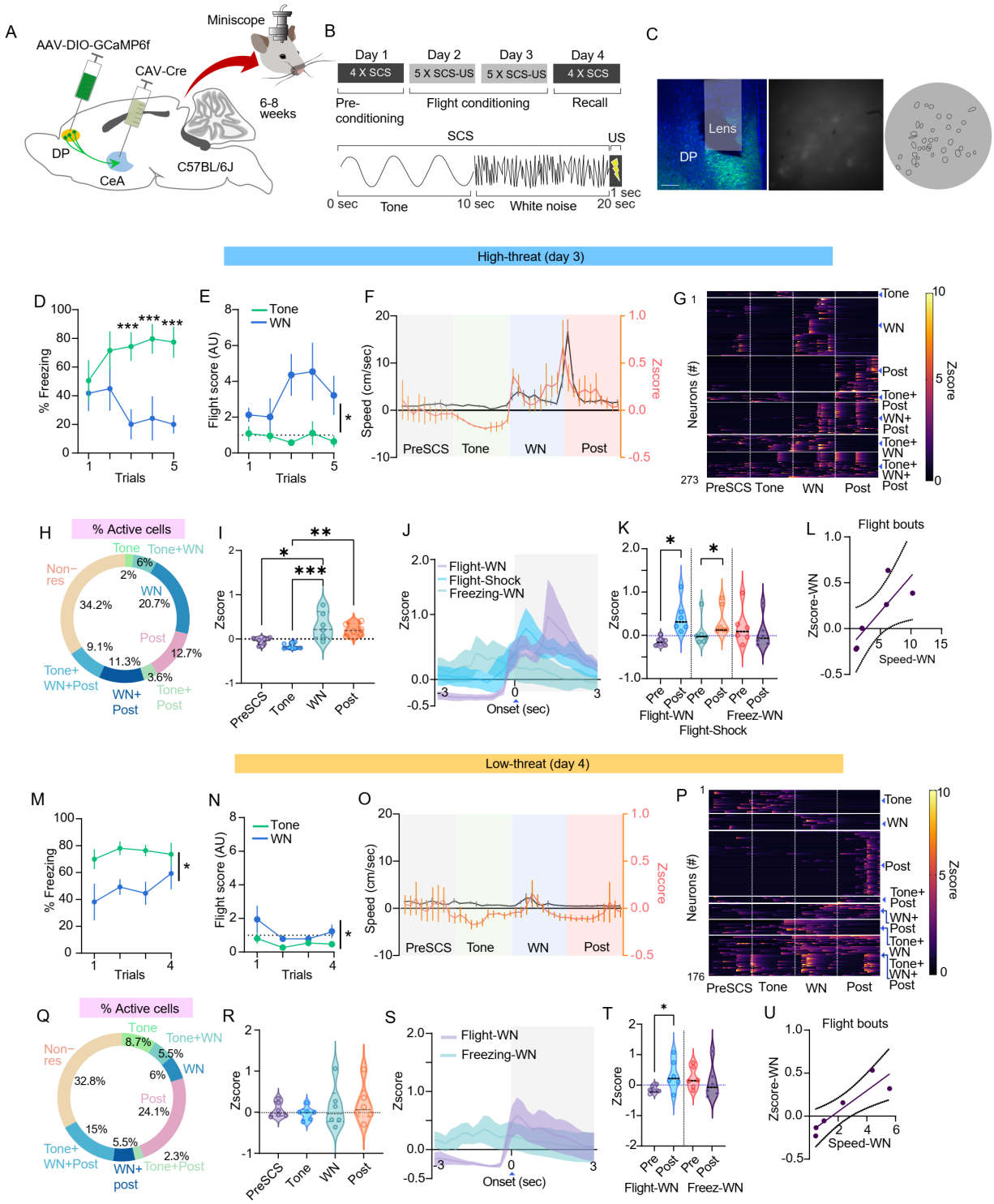

Figure 2: DP-to-CeA projecting cells are activated by high fear states.

A, Schematic of the intersectional strategy used to record DP-to-CeA projector activity (N = 6 mice).

176 **B**, Implanted mice were subjected to a fear conditioning paradigm designed to elicit conditioned
177 freezing and flight.
178 **C**, *Left*, Representative GCaMP6f expression with lens placement in the DP (scale bar = 500
179 μm). *Right*, miniscope field-of-view (raw and post cell extraction).
180 **D,** Trial-wise freezing in the high-threat context. Two-way ANOVA, Trial x Stimuli, $F_{(4, 20)} = 4.354$,
181 $p = 0.01$, followed by Bonferroni's post-hoc test. ***$p < 0.001$. Data shown as means ± s.e.m.
182 **E,** Trial-wise flight in the high-threat context. Two-way ANOVA, Trial x Stimuli, $F_{(4, 20)} = 2.08$, $p =$
183 0.12, Stimuli, $F_{(1, 5)} = 13.49$, $p = 0.014$, Trial, $F_{(4, 20)} = 0.933$, $p = 0.46$. Data shown as means ±
184 s.e.m.
185 **F**, Z-scored neuronal activity and speed on the last trial in the high-threat context (n = 273
186 neurons). Data shown as means ± s.e.m.
187 **G**, Heatmap of neuronal activity during the last trial in the high-threat context (273 neurons from
188 6 mice).
189 **H,** Percentages of neurons activated (neurons with peaks ≥3 s.d. above baseline) during
190 different cue periods in the high-threat context.
191 **I**, Z-score of preSCS, tone and WN and post-shock (post) of the DP-to-CeA population in the
192 high-threat context (from all trials, Ordinary one-way ANOVA, $F_{(3,20)} = 9.33$, $p < 0.001$, followed
193 by Bonferroni's post-hoc test, *P < 0.05, **P < 0.005, ***P < 0.001). Violin plots indicate median,
194 interquartile range, and the distribution of individual data points.
195 **J**, Neuronal activity aligned at the onset of WN-induced freezing and flight, and shock-induced
196 flight in the high-threat context. Data shown as means ± s.e.m.
197 **K**, Neuronal population activity 3 s before and after the onset of freezing and flight responses
198 (Paired t-test flight-WN, t=3.28, df=5, *p<0.05; Mann-Whitney test, flight-shock, *p = 0.0411;
199 Paired t-test freezing-WN, t=1.778, df=5, p=0.13). Violin plots indicate median, interquartile
200 range, and the distribution of individual data points.

L, Spearman correlation of neuronal activity and speed aligned to WN-induced flight bouts (r = 0.94, 95% CI = 0.003864 to 0.1503, *p < 0.05, each point represents one sec).

M, Trial-wise freezing in the low-threat context. Two-way ANOVA, Trial x Stimuli, $F_{(3, 15)}$ = 0.5806, p = 0.63, Stimuli, $F_{(1, 5)}$ = 11.73, p = 0.018, Trial, $F_{(3, 15)}$ = 0.83, p = 0.49. Data shown as means ± s.e.m.

N, Trial-wise flight in the low-threat context. Two-way ANOVA, Trial x Stimuli, $F_{(3, 15)}$ = 1.58, p = 0.23, Stimuli, $F_{(1, 5)}$ = 8.12, p = 0.035, Trial, $F_{(3, 15)}$ = 1.42, p = 0.27. Data shown as means ± s.e.m.

O, Z-scored neuronal population activity and speed on the last trial in the low-threat context. Data shown as means ± s.e.m.

P, Heatmap of Z-scores from active neurons during the last trial in the low-threat context (176 neurons from 6 mice).

Q, Percentages of neurons activated (neurons with peaks ≥3 s.d. above baseline) during different cue periods in the low-threat context.

R, Z-score of preSCS, tone and WN and post-cue (post) of the entire DP-to-CeA population in the low-threat context (from all trials, Ordinary one-way ANOVA, effect of stimuli $F_{(3,20)}$ = 0.39, p = 0.75). Violin plots indicate median, interquartile range, and the distribution of individual data points.

S, Neuronal activity aligned to the onset of WN-induced freezing and flight in the low-threat context. Data shown as means ± s.e.m.

T, Neuronal activity aligned to the onset of freezing and flight responses (Paired t-test flight-WN, t=2.58, df=5, *p<0.05; flight-post, t=0.8493, df=5, p = 0.43; freezing-WN, t=0.8493, df=5, p=0.43). Violin plots indicate median, interquartile range, and the distribution of individual data points.

U, Spearman correlation of neuronal activity and speed aligned to WN-induced flight bouts (r = 0.94, 95% CI = 0.04251 to 0.2010, *p < 0.05. Each point represents one sec).

227

228 **DP-to-CeA neurons mediate avoidance**

229 The prevalence of DP-to-CeA neurons active in the high-threat context suggests a functional role
230 for this pathway in negative-valence related behaviours. We first tested this idea using
231 chemogenetic manipulations of DP-to-CeA neurons in standard avoidance paradigms used to
232 assay anxiety-like states: the open field test (OFT) and the elevated plus maze (EPM). We used
233 an intersectional targeting strategy to express either inhibitory (hM4Di-mCherry) or excitatory
234 (hM3Dq-mCherry) DREADDs in the DP-to-CeA pathway, with an mCherry group serving as a
235 CNO control (**Fig. 3A–C**). DREADD-mediated inhibition of the DP-to-CeA pathway increased the
236 time spent and number of entries in the centre zone of the OFT (**Fig. 3D, F, and G**), as well as
237 increasing the number of entries into the open arm of the EPM (**Fig. 3E, I, and J**) without affecting
238 the total distance travelled (**Fig. 3H**). By contrast, chemogenetic stimulation of this pathway did
239 not induce avoidance behaviour in either assay. These findings suggest that the DP-to-CeA
240 pathway is necessary but not sufficient for innate avoidance behaviour.

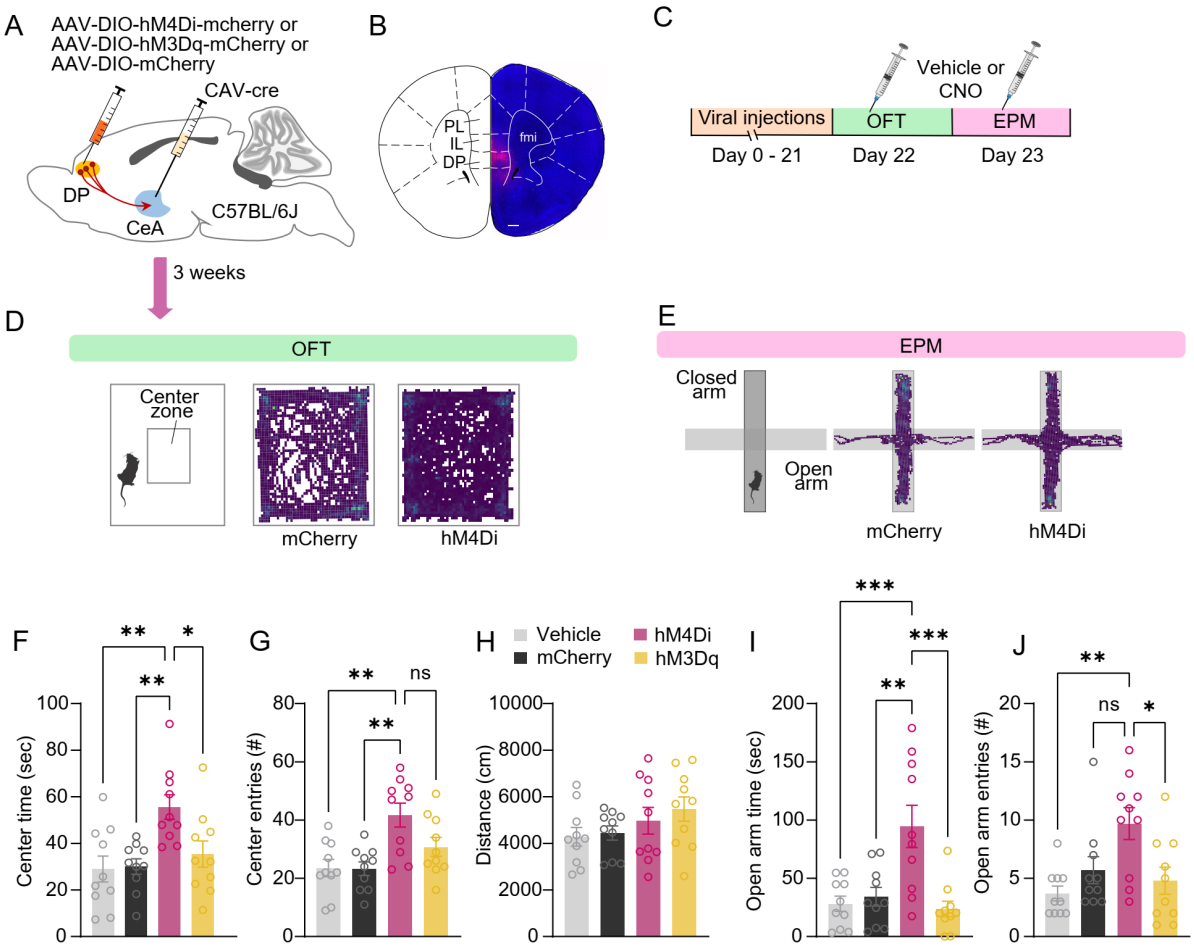

Figure 3: Chemogenetic inhibition of DP-to-CeA pathway reduces avoidance.

A, Intersectional strategy used for chemogenetic manipulation of the DP-to-CeA pathway.

B, Representative mCherry expression in the DP (scalebar = 500 µm).

C, Mice from control (hM4Di-mCherry + vehicle, N = 10; mCherry + CNO, N = 10) and DREADD (hM4Di-mCherry, N = 10; hM3Dq-mCherry, N = 10) groups were subjected to the OFT and EPM 30 min after CNO (5 mg/kg) or vehicle injection.

D, Representative activity plots of mCherry + CNO and hM4Di + CNO mice in the OFT.

E, Representative activity plots of mCherry + CNO and hM4Di + CNO mice in the EPM.

F, Inhibition of DP-to-CeA pathway significantly increased the time spent in the centre zone (One-way ANOVA, $F_{(3,36)} = 6.06$ $p = 0.01$). Bonferroni's post-hoc test. *$p < 0.05$, **$p < 0.01$.

252 **G**, Inhibition of DP-to-CeA pathway significantly increased the number of entries in the centre
253 zone (One-way ANOVA, $F_{(3,36)} = 7.158$, $p = 0.0007$). Bonferroni's post-hoc test. $^{**}p < 0.01$.
254 **H**, DREADD manipulations did not alter distance travelled in the OFT (One-way ANOVA, $F_{(3,36)}$
255 $= 1.36$, $p = 0.270$).
256 **I**, inhibition of the DP-to-CeA pathway significantly increased open-arm time in the EPM (One-
257 way ANOVA, $F_{(3,36)} = 9.22$, $p = 0.0001$). Bonferroni's post-hoc test. $^{*}p < 0.05$; $^{**}p < 0.01$; $^{***}p <$
258 0.001.
259 **J**, inhibition of the DP-to-CeA pathway significantly increased open-arm entries in the EPM
260 (One-way ANOVA, $F_{(3,36)} = 5.47$, $p = 0.003$). Bonferroni's post-hoc test. $^{*}p < 0.05$; $^{**}p < 0.01$;
261 $^{***}p < 0.001$.
262 All values represented as mean ± s.e.m.
263
264 **DP-to-CeA neurons mediate flight**
265 To study the necessity of the DP-to-CeA pathway in other forms of defensive behaviour, we
266 performed loss-of-function studies using optogenetics in the OFT and SCS-FC (**Fig. 4 A–F; Fig.**
267 **S4**). We injected a Cre-dependent vector carrying eNpHR or EYFP control into the DP, and a
268 retrograde CAV2-Cre vector into the CeA of C57BL/6J mice (**Fig. 4A; Fig. S4A**). Inhibition of DP-
269 to-CeA terminals significantly increased the time spent in, and number of entries into, the centre
270 zone of the OFT, but did not affect locomotor activity, consistent with chemogenetic inhibition
271 (**Fig. S4C–E**). We then used a within-subjects experimental design in the SCS-FC paradigm, with
272 optogenetic stimulation during half of the trials (**Fig. S4B**). In the high-threat context, inhibition of
273 DP-to-CeA terminals significantly reduced WN-induced flight (**Fig. 4E; Fig. S4G, H**). Interestingly,
274 inhibiting these terminals reduced freezing to the tone, yet also elevated freezing during the WN
275 period, demonstrating cue-specific reduction in defensive response intensity but not a complete
276 inhibition of fear (**Fig. 4D; Fig. S4F**).[22,23]. Optogenetic inhibition had no effect on defensive

277 behaviour in the low-threat context (**Fig. 4F; Fig. S4I–K)**, further supporting the context-
278 dependent function of the DP-to-CeA pathway.
279
280 To study the sufficiency of the DP-to-CeA pathway in mediating flight, anxiety, and aversive
281 behaviour, we performed optogenetic gain-of-function studies (**Fig. 4G–R; Figs. S5–S8**).
282 Optogenetic activation of DP-to-CeA terminals using a non-cell type specific intersectional
283 approach (**Fig. S5A**) did not elicit significant changes in negative valence behaviours (**Fig. S5B–**
284 **J**). Stimulation of DP terminals in the CEA expressing ChR2 under the control of a CaMKIIa
285 promoter (**Fig. S6A**) elicited a significant avoidance response (**Fig. S6B, C**); however, there was
286 no significant effect on freezing and flight responses in either threat context (**Fig. S6D–G**).
287
288 The lack of effect of these manipulations on defensive behaviour could be due to functional
289 heterogeneity in the DP-to-CEA pathway (**Fig. 1J**). Therefore, we separately targeted the Vglut1+
290 and Vglut2+ subpopulations and stimulated axon terminals in the CEA (**Fig. 4G; Figs. S7, S8**).
291 Stimulation of Vglut1+ terminals induced real-time place preference (**Fig. S7B, C**), and a reduction
292 in cue-induced freezing (**Fig. S7D, F**), but it had no effect on conditioned flight responses (**Fig.**
293 **S7E, G**). Optogenetic activation of Vglut2+ terminals in the CeA (**Fig. S8A–B**), however, induced
294 significant place avoidance (**Fig. S8C**), and a significant decrease in the number of centre entries
295 in the OFT (**Fig. S8D, E**). Stimulation of Vglut2+ terminals also significantly reduced freezing (**Fig.**
296 **4I, L; Fig. S8F, I**), and significantly elevated flight responses in both contexts (**Fig. 4J, K, and M;**
297 **Fig. S8G, H, and J**).
298
299 We next tested the effects of Vglut2+ terminal stimulation on flight responses in the high-threat
300 context in absence of footshock (**Fig. 4N–R**). Optogenetic stimulation during WN significantly
301 reduced freezing (**Fig. 4N, O**), and increased flight responses (**Fig. 4P–R**). Together, these data

302 demonstrate that the DP-to-CeA pathway is necessary and sufficient for conditioned flight
303 responses.
304
305 **DP neurons control CeM outputs**
306 To investigate how DP neurons might impact flight behaviour via the CeM, we first asked whether
307 DP-to-CeA projections differentially innervate defined cell types in the CeM that are known to
308 mediate defensive behaviour, as in the CeL[2] (**Fig. S9A–I**). There were many labelled terminals
309 near both somatostatin (SOM)+ and corticotrophin releasing hormone (CRH)+ somata in the CeM
310 (**Fig. S9B**), and DP fibre stimulation resulted in a strong induction of either a monophasic inward
311 synaptic current or a biphasic inward/outward synaptic current in both SOM+ and CRH+ neurons
312 in the CeM (**Fig. S9D, F, and I**), but not CeL (**Fig. S9E, H**). These optogenetically-evoked
313 responses were blocked by bath application of the AMPA receptor antagonist DNQX (**Fig. S9G**).
314 These findings confirm the presence of functional glutamatergic DP projections to the CeM but
315 also suggest that this pathway controls flight behaviour via a mechanism distinct from that which
316 was previously described in the CeL.
317
318 CeM output neurons can be classified by their action potential firing properties,[24–26] with distinct
319 subclasses influencing behavioural threat responding via their projections to known targets within
320 the periaqueductal gray (PAG).[26–28] In particular, burst firing and regular firing neurons innervate
321 the dorsolateral and lateral columns of the PAG (dl/l PAG) involved in flight responses.[26,29,30] We
322 tested if DP innervation targeted physiologically defined CeM neuronal populations. We classified
323 DP-excited CeM neurons as regular spiking, bursting, or late-firing (**Fig 5A–C; Fig. S9J**).
324 Optogenetic stimulation of DP terminals in the CeA primarily evoked EPSCs in burst firing and
325 regular firing neurons, while late-firing neurons were only rarely excited (**Fig. 5C**), suggesting that
326 the DP excites CeM projections to PAG columns linked to flight behaviour.
327

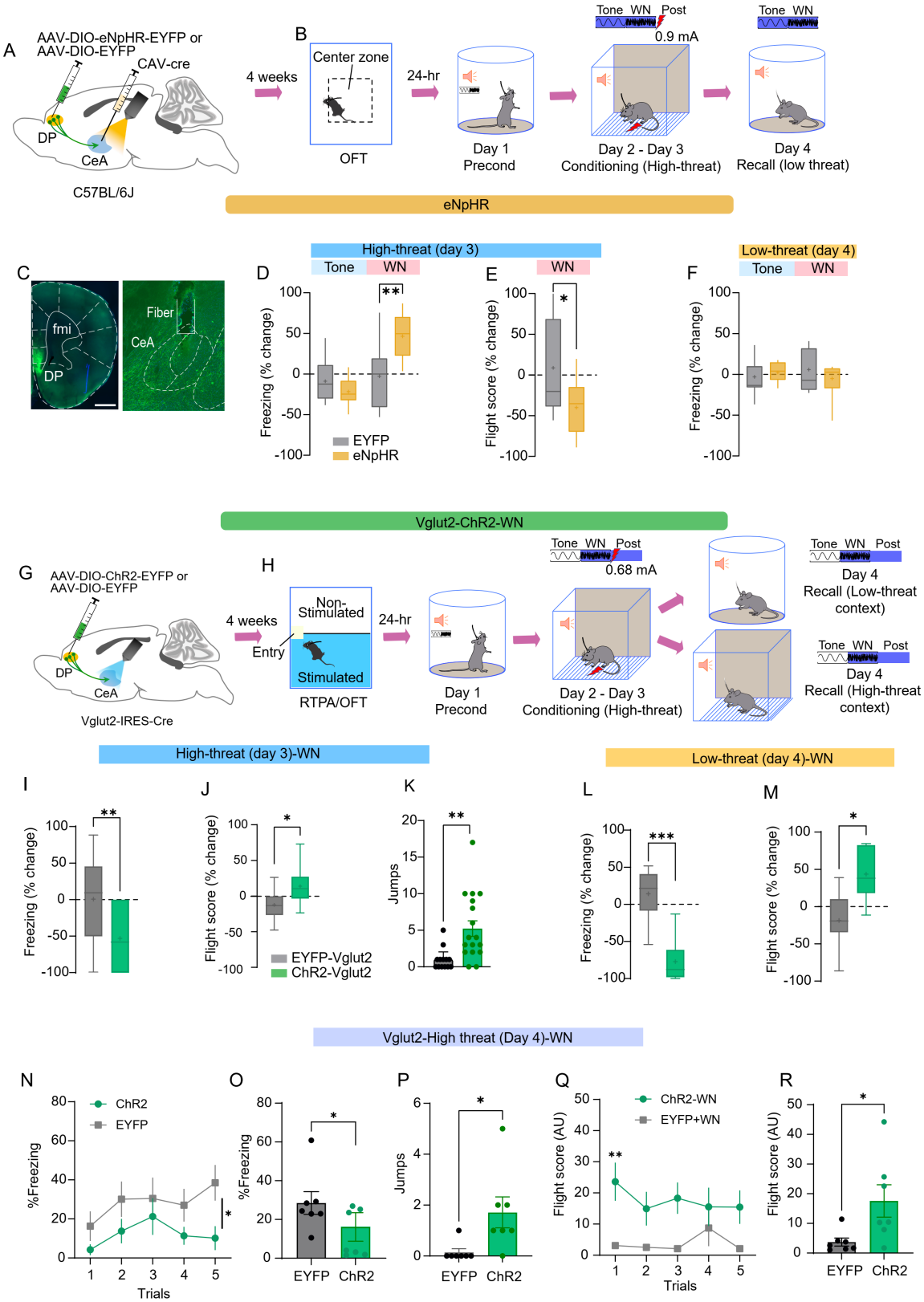

Figure 4. Optogenetic modulation of the DP-to-CeA pathway regulates flight.

330 **A**, Schematic of intersectional targeting strategy for optogenetic inhibition of DP-to-CeA
331 pathway.
332 **B**, Experimental timeline for optogenetic inhibition experiments.
333 **C**, Representative images of eNpHR-EYFP expression in DP and fibre stub placement in CeA
334 (scalebar = 500 μm).
335 **D**, Effect of optogenetic inhibition in EYFP (N = 9) and eNpHR (N = 9) groups on freezing (LED-
336 on vs LED-off) in the high-threat context (EYFP vs eNpHR, Mann-Whitney, ** $p < 0.01$).
337 **E**, Effect of optogenetic inhibition in EYFP (N = 9) and eNpHR (N = 9) groups on flight scores
338 (LED-on vs LED-off) in the high-threat context (EYFP vs eNpHR, Mann-Whitney, * $p < 0.05$).
339 **F**, Effect of optogenetic inhibition in EYFP (N = 9) and eNpHR (N = 9) groups on freezing (LED-
340 on vs LED-off) in the low-threat context (EYFP vs eNpHR, Mann-Whitney, n.s.)
341 **G**, Schematic of viral injection and strategy for optogenetic stimulation of DP-to-CeA pathway.
342 **H**, Experimental timeline for optogenetic stimulation experiments.
343 **I**, Effect of optogenetic stimulation in EYFP control (N = 13) or Vglut2-ChR2 (N = 17) groups on
344 freezing (LED-on vs LED-off) in the high-threat context (Unpaired t-test, t=2.46, df=28, *p =
345 0.02).
346 **J**, Effect of optogenetic stimulation in EYFP control (N = 13) or Vglut2-ChR2 (N = 17) groups on
347 flight scores (LED-on vs LED-off) in the high-threat context (Unpaired t-test, t=2.262, df=28, *p =
348 0.0316).
349 **K**, Effect of optogenetic stimulation in EYFP control (N = 13), and Vglut2-ChR2 (N = 17) groups
350 on total escape jumps in the high-threat context (Unpaired t-test, t=3.383, df=28, **p = 0.0021).
351 **L**, Effect of optogenetic stimulation in EYFP control (N = 6) and Vglut2-ChR2 (N = 10) groups on
352 freezing (LED-on vs LED-off) in the low-threat context (Unpaired t-test, t=5.046, df=14, ***p <
353 0.001).
354 **M**, Effect of optogenetic stimulation in EYFP control (N = 6) and Vglut2-ChR2 (N = 10) groups
355 on flight scores (LED-on vs LED-off) in the low-threat context (Unpaired t-test, t=2.845, df=14,
356 *p < 0.05).
357 **N**, Trial-wise freezing during optogenetic stimulation in EYFP control (N = 7) and Vglut2-ChR2
358 (N = 7) groups during recall in the high-threat context. (Two-way ANOVA, Group x trial, $F_{(4, 48)}$ =
359 0.644, P=0.633, main effect of Group, $F_{(1,12)}$ = 4.874, P=0.0475).
360 **O**, Average freezing during optogenetic stimulation in EYFP control (N = 7) and Vglut2-ChR2 (N
361 = 7) groups during recall in the high-threat context (Unpaired t-test, t=2.208, df=12, *$p < 0.05$).

362 **P**, Number of escape jumps during optogenetic stimulation in EYFP control (N = 7) and Vglut2-
363 ChR2 (N = 7) groups during recall in the high-threat context (Unpaired t-test, t=2.524, df=12, *p
364 < 0.05)
365 **Q**, Trial-wise flight score during optogenetic stimulation in Vglut2 EYFP control (N = 7) and
366 Vglut2 ChR2 (N = 7) groups during recall in the high-threat context (Two-way ANOVA, Trial x
367 Group, $F_{(4, 48)} = 2.738$, P=0.0393, main effect of Group, $F_{(1,12)} = 6.06$, P = 0.0299, followed by
368 Bonferroni's multiple comparisons test. **p < 0.01).
369 **R**, Average flight score during optogenetic stimulation in Vglut2 EYFP control (N = 7) and Vglut2
370 ChR2 (N = 7) groups during recall in the high-threat context (Unpaired t-test, t=2.462, df=12, *p
371 < 0.05).
372 Box and whisker plots indicate median, interquartile range, and min. to max. of the distribution,
373 crosses indicate means. Values in bar graphs and line graphs represented as mean ± s.e.m.
374

375 To directly test this hypothesis, we first labelled the neuroanatomical pathway by injecting an
376 anterograde transneuronal AAV1-Cre vector into the DP region and a Cre-dependent mCherry-
377 expressing vector into the CeM (**Fig. 5D**). The projection topography of the labelled CeM neurons
378 in the PAG revealed that the lateral PAG, known to regulate flight,[28] had the highest density of
379 mCherry+ fibres (**Fig. 5E–G**). We then labelled CeM projections to different columns of the PAG
380 and performed whole cell patch clamp recordings while optogenetically stimulating Vglut2+ DP
381 afferents in CeM (**Fig. 5H**). We observed that CeM projections to the dl/l PAG have larger
382 monosynaptic excitatory currents than projections to the vlPAG in response to stimulation of DP
383 terminals (**Fig. 5I–J**), despite there being no preferential innervation bias between the projection
384 pathways (**Fig. 5K**). These data support the hypothesis that the DP promotes flight through
385 excitation of CEA output neurons to columns of PAG known to be important for flight behaviour.
386

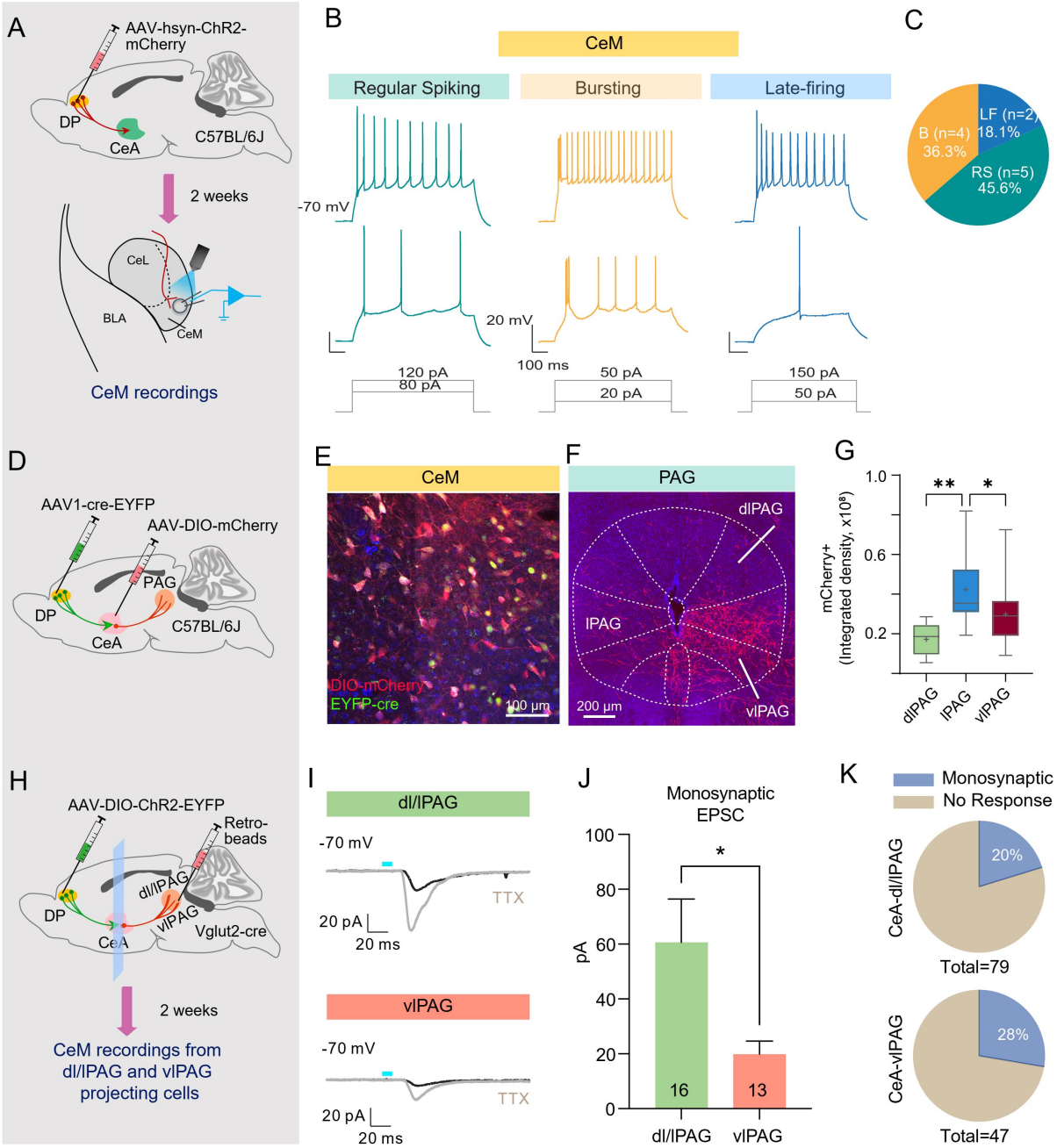

Figure 5. DP-to-CeA neurons exert excitatory control over CeM neurons projecting to PAG.

A, Injection targeting and recording strategy.

B, Representative evoked synaptic responses in CeM cells by photostimulation of DP axonal fibres and following DNQX application in voltage-clamp (-70 mV).

C, Proportion of DP-excited CeM neurons classified by firing patterns (N = 11 cells from 4 mice).

394 **D**, Schematic of viral targeting strategy to map the DP innervating CeM neurons projecting to
395 PAG subregions.
396 **E**, Representative image showing expression of EYFP-cre (green) and DIO-mcherry colocalized
397 in the CeM.
398 **F**, Representative image showing mcherry+ terminals in the PAG subregions.
399 **G**, Morphometric analysis showing that lPAG receives significantly higher DP-CeM mCherry+
400 terminals (repeated measure One way-ANOVA, $F_{(2,36)} = 12.50$, $P = 0.0006$, followed by
401 Bonferroni's multiple comparison test, $*p < 0.05$, $**p < 0.01$). Box and whisker plots indicate
402 median, interquartile range, and crosses indicate means.
403 **H**, Schematic of targeting and recording strategy.
404 **I**, Representative evoked synaptic responses in dl/lPAG (*top*) and vlPAG (*bottom*) projecting
405 CeM cells by photostimulation of DP axonal fibres and TTX application.
406 **J**, Average amplitude of evoked monosynaptic EPSCs was significantly higher in dl/lPAG (N =
407 16 cells from 10 mice) as compared to vlPAG (N = 13 cells from 7 mice) projecting CeM
408 neurons (Mann Whitney test, $*p = 0.0367$). Values represented as mean ± s.e.m.
409 **K**, Proportion CeM neurons with EPSCs by DP terminals stimulation, classified by their
410 projections to dl/l PAG (20%, *top*) and vlPAG (28%, *bottom*).
411
412

413 **Discussion**

414 Here, we define the function of a novel top-down pathway from the DP region of the mPFC directly
415 to the CeA in the control of defensive behaviour. This non-canonical corticolimbic pathway is
416 distinct from the well-studied reciprocal pathway between the prelimbic and infralimbic cortices
417 and the basolateral amygdala and is specifically activated in high-threat situations. Glutamatergic
418 DP neurons exert their influence via projections to the CeM, the amygdalar output nucleus known
419 for coordinating complex responses to threats. These findings have important implications for
420 understanding the basic neurobiology of threat processing.
421

422 This adds to a growing body of literature defining the CeA as a vital limbic brain structure that
423 integrates complex sensory information to generate survival behaviour.[23,31–33] It is hypothesized

424 that CeM output neurons control freezing through projections to the PAG,[28,34] and our results
425 demonstrate for the first time that the CeM is also important for flight. DP-to-CeA projections target
426 specific classes of CeM neurons that project to flight centres in the PAG, with weaker inputs to
427 neuronal classes linked to freezing.[26] Our study supports the idea that top-down integration of
428 information in the dl/l PAG contributes to defensive action selection to threat.[35,36] It has been
429 demonstrated that CeL circuit activity is regulated by local recurrent inhibitory interactions,[2,37,38]
430 and this mutual inhibition motif is likely important for rapid action selection. Future studies should
431 investigate whether a similar "winner-take-all" motif is used in the CeM to select between freezing
432 versus flight responses.
433
434 Learned fear is traditionally assayed using freezing, control of which involves the well-established
435 mPFC-basolateral amygdala-CeA pathway.[39] Previous research has shown that IL projections to
436 the basolateral amygdala and intercalated cell masses effectively operate to inhibit fear by
437 supporting fear extinction.[40,41] In contrast, the DP-to-CeA pathway defined here operates under
438 high-threat conditions and is necessary for generating flight. The context- and cue-specificity of
439 DP-to-CeA activation and function is consistent with the known role of context and salience in
440 defensive action selection.[42–44] Our findings therefore implicate the importance of the mPFC in
441 executive control over high-intensity fear responses and may lead to a better understanding of
442 the cortical dysfunction observed in PTSD and panic disorder.[14]
443
444 **References**

445 1. Fonzo, G. A. *et al.* PTSD psychotherapy outcome predicted by brain activation during
446 emotional reactivity and regulation. *Am. J. Psychiatry* **174**, 1163–1174 (2017).
447 2. Fadok, J. P. *et al.* A competitive inhibitory circuit for selection of active and passive fear
448 responses. *Nature* **542**, 96–99 (2017).
449 3. Roelofs, K. Freeze for action: Neurobiological mechanisms in animal and human

450 freezing. *Philos. Trans. R. Soc. Lond., B, Biol. Sci.* **372** (2017).

451 4. Fanselow, M. S., Hoffman, A. N. & Zhuravka, I. Timing and the transition between modes
452 in the defensive behavior system. *Behav. Processes* **166**, 103890 (2019).

453 5. Blanchard, D. C. & Blanchard, R. J. Defensive behaviors, fear, and anxiety. In *Handbook*
454 *of anxiety and fear.* 63–79 (Elsevier Academic Press, 2008). doi:10.1016/S1569-
455 7339(07)00005-7.

456 6. Perusini, J. N. & Fanselow, M. S. Neurobehavioral perspectives on the distinction
457 between fear and anxiety. *Learn. Mem.* **22**, 417–425 (2015).

458 7. Johnson, P. L., Truitt, W. A., Fitz, S. D., Lowry, C. A. & Shekhar, A. Neural pathways
459 underlying lactate-induced panic. *Neuropsychopharmacol.* **33**, 2093–2107 (2008).

460 8. Münsterkötter, A. L. *et al.* Spider or no spider? Neural correlates of sustained and phasic
461 fear in spider phobia. *Depress. Anxiety* **32**, 656–663 (2015).

462 9. Mobbs, D. *et al.* From threat to fear: The neural organization of defensive fear systems in
463 humans. *J. Neurosci.* **29**, 12236–12243 (2009).

464 10. Tromp, D. P. M. *et al.* Reduced structural connectivity of a major frontolimbic pathway in
465 generalized anxiety disorder. *Arch. Gen. Psychiatry* **69**, 925–934 (2012).

466 11. Marek, R., Strobel, C., Bredy, T. W. & Sah, P. The amygdala and medial prefrontal
467 cortex: Partners in the fear circuit. *J. Physiol.* **591**, 2381–2391 (2013).

468 12. Senn, V. *et al.* Long-range connectivity defines behavioral specificity of amygdala
469 neurons. *Neuron* **81**, 428–437 (2014).

470 13. Karalis, N. *et al.* 4-Hz oscillations synchronize prefrontal-amygdala circuits during fear
471 behavior. *Nat. Neurosci.* **19**, 605–612 (2016).

472 14. Andrewes, D. G. & Jenkins, L. M. The role of the amygdala and the ventromedial
473 prefrontal cortex in emotional regulation: Implications for post-traumatic stress disorder.
474 *Neuropsychol. Rev.* **29**, 220–243 (2019).

475 15. De Franceschi, G., Vivattanasarn, T., Saleem, A. B. & Solomon, S. G. Vision guides

476 selection of freeze or flight defense strategies in mice. *Curr. Biol.* **26**, 2150–2154 (2016).
477 16. Wang, W. *et al.* Coordination of escape and spatial navigation circuits orchestrates
478 versatile flight from threats. *Neuron* **109**, 1–13 (2021).
479 17. Mcdonald, A. J. Cortical pathways to the mammalian amygdala. *Prog. Neurobiol.* **55**,
480 257–332 (1998).
481 18. Kataoka, N., Shima, Y., Nakajima, K. & Nakamura, K. A central master driver of
482 psychosocial stress responses in the rat. *Science* **367**, 1105–1112 (2020).
483 19. Anastasiades, P. G. & Carter, A. G. Circuit organization of the rodent medial prefrontal
484 cortex. *Trends Neurosci.* **44**, 550–563 (2021).
485 20. Fremeau, R. T. *et al.* The expression of vesicular glutamate transporters defines two
486 classes of excitatory synapse. *Neuron* **31**, 247–260 (2001).
487 21. Borkar, C. D. & Fadok, J. P. A novel pavlovian fear conditioning paradigm to study
488 freezing and flight behavior. *J Vis Exp* 1–13 (2021). doi:10.3791/61536.
489 22. Anderson, D. J. & Adolphs, R. A framework for studying emotions across species. *Cell*
490 **157**, 187–200 (2014).
491 23. Fadok, J. P., Markovic, M., Tovote, P. & Lüthi, A. New perspectives on central amygdala
492 function. *Curr. Opin. Neurobiol.* **49**, 141–147 (2018).
493 24. Dumont, É. C., Martina, M., Samson, R. D., Drolet, G. & Paré, D. Physiological properties
494 of central amygdala neurons: Species differences. *Eur. J. Neurosci.* **15**, 545–552 (2002).
495 25. Duvarci, S., Popa, D. & Paré, D. Central amygdala activity during fear conditioning. *J.*
496 *Neurosci.* **31**, 289–294 (2011).
497 26. Li, J. N. & Sheets, P. L. The central amygdala to periaqueductal gray pathway comprises
498 intrinsically distinct neurons differentially affected in a model of inflammatory pain. *J.*
499 *Physiol.* **596**, 6289–6305 (2018).
500 27. Rizvi, T. A., Ennis, M., Behbehani, M. M. & Shipley, M. T. Connections between the
501 central nucleus of the amygdala and the midbrain periaqueductal gray: Topography and

502 reciprocity. *J. Comp. Neurol.* **303**, 121–131 (1991).
503 28. Tovote, P. *et al.* Midbrain circuits for defensive behaviour. *Nature* **534**, 206–212 (2016).
504 29. Bandler, R. & Carrive, P. Integrated defence reaction elicited by excitatory amino acid
505 microinjection in the midbrain periaqueductal grey region of the unrestrained cat. *Brain*
506 *Res.* **439**, 95–106 (1988).
507 30. Behbehani, M. M. Functional characteristics of the midbrain periaqueductal gray. *Prog.*
508 *Neurobiol.* **46**, 575–605 (1995).
509 31. Keifer, O. P., Hurt, R. C., Ressler, K. J. & Marvar, P. J. The physiology of fear:
510 Reconceptualizing the role of the central amygdala in fear learning. *Physiology* **30**, 389–
511 401 (2015).
512 32. Ressler, R. L. & Maren, S. Synaptic encoding of fear memories in the amygdala. *Curr.*
513 *Opin. Neurobiol.* **54**, 54–59 (2019).
514 33. Kong, M. S. & Zweifel, L. S. Central amygdala circuits in valence and salience
515 processing. *Behav. Brain Res.* **410**, 113355 (2021).
516 34. Viviani, D. *et al.* Oxytocin selectively gates fear responses through distinct outputs from
517 the central amygdala. *Science* **333**, 104–107 (2011).
518 35. Evans, DA. *et al*. A synaptic threshold mechanism for computing escape decisions.
519 *Nature* **558**, 46–76 (2009).
520 36. Wang, W. *et al.* Dorsal premammillary projection to periaqueductal gray controls escape
521 vigor from innate and conditioned threats. *Elife* **10**, 1–30 (2021).
522 37. Li, H. *et al.* Experience-dependent modification of a central amygdala fear circuit. *Nat.*
523 *Neurosci.* **16**, 332–339 (2013).
524 38. Hunt, S., Sun, Y., Kucukdereli, H., Klein, R. & Sah, P. Intrinsic circuits in the CeL. *eNeuro*
525 **4**, 1–18 (2017).
526 39. Tovote, P., Fadok, J. P. & Lüthi, A. Neuronal circuits for fear and anxiety. *Nat. Rev.*
527 *Neurosci.* **16,** 317–331 (2015).

528 40. Quirk, G. J., Likhtik, E., Pelletier, J. G. & Paré, D. Stimulation of medial prefrontal cortex
529 decreases the responsiveness of central amygdala output neurons. *J. Neurosci.* **23**,
530 8800–8807 (2003).
531 41. Bukalo, O. *et al.* Prefrontal inputs to the amygdala instruct fear extinction memory
532 formation. *Sci. Adv.* **1**, 1–9 (2015).
533 42. Hersman, S., Allen, D., Hashimoto, M., Brito, S. I. & Anthony, T. E. Stimulus salience
534 determines defensive behaviors elicited by aversively conditioned serial compound
535 auditory stimuli. *Elife* **9**, (2020).
536 43. Dong, P. *et al.* A novel cortico-intrathalamic circuit for flight behavior. *Nat. Neurosci.* **22**,
537 941–949 (2019).
538 44. Totty, M. S. *et al.* Behavioral and brain mechanisms mediating conditioned flight behavior
539 in rats. *Sci. Rep.* **11**, 1–15 (2021).
540
541

542 **Methods**

543 **Animals.** Male and female C57BL/6J (Stock No: 000664, Jackson laboratories, USA) mice aged
544 8-12 weeks were used. CRH-IRES-Cre (Stock Number: 012704), SOM-IRES-Cre (Stock No:
545 013044), Vglut1-IRES-Cre (Slc17a7-IRES2-Cre-D, Stock No: 023527) and Vglut2-ires-cre (Stock
546 Number: 028863) mice were used for *in-vitro* electrophysiology (aged 5-8 weeks), and to
547 determine anatomical connectivity between DP and CeA, and CeA and PAG. For Vglut
548 subpopulation tracing, Vglut1-IRES2-Cre and Vglut2-IRES-cre (Stock Number: 028863) mouse
549 lines were used. All Cre-driver lines were fully backcrossed to C57BL/6J. All mice were individually
550 housed on a 12-hr light/dark cycle with *ad libitum* food and water. Behavioural experiments were
551 performed during the light phase. Animals were habituated by cupping the mouse in hand for 5
552 minutes each day for 2 days, before the start of the experiment. All animal procedures were
553 performed in accordance with institutional guidelines and were approved by the Tulane University
554 Institutional Animal Care & Use Committee.

555 **Viruses**

556 For Cre-dependent expression of channelrhodopsin (ChR2), we used AAV5-EF1a-DIO-
557 hChR2(H134R)-EYFP-WPRE-HGHpa (Addgene 20298, a gift from Karl Deisseroth). For Cre-
558 dependent expression of halorhodopsin (eNpHR), we used AAV5-EF1a-DIO-eNpHR3.0-EYFP
559 (Addgene 26966, a gift from Karl Deisseroth). Control mice for optogenetic experiments were
560 injected with AAV5-EF1a-DIO-EYFP (Addgene 27056, a gift from Karl Deisseroth). For Cre-
561 dependent expression of excitatory DREADDs, we used AAV5-hSyn-DIO-hM3D(Gq)-mCherry
562 (Addgene 44361, a gift from Bryan Roth). For Cre-dependent expression of inhibitory DREADDs,
563 we used AAV-hSyn-DIO-hM4D(Gi)-mCherry (Addgene 44362, a gift from Bryan Roth). For Cre-
564 dependent GCaMP6f expression, we used AAV5-CAG-Flex-GcaMP6f-WPRE-SV40 (Addgene
565 100835, a gift from Douglas Kim & GENIE Project). To express Cre in C57BL/6J mice, we used

566 retrograde transporting canine adenovirus type 2 carrying Cre-recombinase (CAV2-Cre, PVM,
567 France).[45] For anterograde neuronal tracing experiments in Vglut1- or Vglut2-cre mouse lines,
568 AAV5-hSyn-DIO-mCherry (Addgene 50459, a gift from Bryan Roth) was injected in the DP.

569 To label CRH+ and SOM+ somata in the CeA for *in-vitro* electrophysiology experiments and
570 anatomical tracing, CRH-IRES-Cre and SOM-IRES-Cre mouse lines were injected with AAV5-
571 EF1a-DIO-EYFP (Addgene 27056, a gift from Karl Deisseroth). In the same mice, we used AAV5-
572 hSyn-hChR2(H134R)-mCherry (Addgene 26976, a gift from Karl Deisseroth) to express ChR2 in
573 the DP for *in-vitro* electrophysiology. To characterize firing patters of CeM neurons (unlabeled)
574 innervated by DP projectors, we used AAV5-hSyn-hChR2(H134R)-mCherry (Addgene 26976, a
575 gift from Karl Deisseroth) in DP. To study the direct effect of Vglut2+ DP projections of PAG
576 projecting CeA neurons using *in-vitro* electrophysiology, we injected AAV5-EF1a-DIO-
577 hChR2(H134R)-EYFP (Addgene 20298, a gift from Karl Deisseroth) in the DP of Vglut2-IRES-cre
578 mice and retrograde beads in PAG subcolumns to label CeM projectors. For anterograde
579 neuronal tracing experiments in Vglut1- or Vglut2-cre mouse lines, AAV5-hSyn-DIO-mCherry
580 (Addgene 50459, a gift from Bryan Roth) was injected in the DP.

581 **Surgery**

582 *Tracers/Virus injections*

583 Mice were deeply anaesthetized using 5% isoflurane (Fluriso, VetOne, Boise, ID) in oxygen-
584 enriched air (OxyVet O2 Concentrator, Vetequip, Pleasanton, CA), followed by a subcutaneous
585 injection of 2 mg/kg meloxicam (OstiLox, VetOne, Boise, ID), and then fixed into a stereotaxic
586 frame (Model 1900, Kopf Instruments, Tujunga, CA) equipped with a robotic stereotaxic targeting
587 system (Neurostar, Germany). Anesthetized mice were maintained on 2-2.5% isoflurane, and a
588 core body temperature was maintained at 36°C using a feedback-controlled DC temperature

589 controller (ATC2000, World Precision Instruments, Sarasota, FL). Eye ointment (GenTeal, Alcon,
590 Switzerland) was applied to the mouse's eyes to prevent dryness. The head was shaved, and the
591 skin was sterilized using Betadine iodine solution (Purdue Products, Stamford, CT). 2% lidocaine
592 (0.1 ml, Lidocaine 2%, VetOne, Boise, ID) was injected subcutaneously at the site of incision and
593 a midline incision was made with a scalpel to expose the skull.

594 For the retrograde neuronal tracings, retrogradely transported beads (0.2 µl, 1:2 diluted with
595 saline, Lumafluor Inc., Durham, NC) were stereotaxically injected into the respective brain
596 regions. We injected CAV2-Cre into the CeA, and Cre-dependent AAV opsins or DREADD
597 vectors into the DP. Approximately 0.4 µl per hemisphere of each vector was delivered bilaterally
598 into the respective brain regions using pulled glass pipettes (tip diameter 10-20 µm, PC-100 puller,
599 Narishige, Japan), connected to a pressure ejector (PDES-Pressure Application System, npi
600 electronic equipment, Germany). AAV-DIO-mcherry was injected into the DP of Vglut1-/Vglut2-
601 IRES-Cre mice for neuronal anterograde tracings. For *in-vitro* electrophysiology, AAV-syn-ChR2-
602 mCherry was injected into the DP and Cre-dependent AAV-DIO-EYFP was injected into the CeA
603 of CRH-IRES-Cre or SOM-IRES-Cre mice. AAV-DIO-ChR2-EYFP was injected into the DP of
604 Vglut1-/Vglut2-IRES-Cre mice. For calcium imaging, C57BL/6J mice were injected unilaterally
605 with CAV2-cre in the CeA and Cre-dependent GCaMP6f in the DP.

606 The CeA coordinates used were: 1.2-1.3 mm posterior to bregma, ±2.8-2.9 mm lateral to the
607 midline and 4.1-4.3 mm below the dura. The DP coordinates used were 1.8-1.9 mm anterior to
608 bregma, ±0.4-0.5 mm lateral to the midline and 3.1-3.2 mm below the dura. The DMH coordinates
609 used were 1.7 mm posterior to bregma, ±0.5 mm lateral to the midline and 5 mm below the dura.
610 The dl/l and vl PAG coordinates used were -4.16 mm (-4.72 mm for vlPAG) posterior to bregma,
611 -0.4 mm lateral to the midline and 2.4 mm (2.7 mm for vlPAG) below the dura.

612 *Fibre implantation for optogenetics*

613 For optogenetic manipulations of behaviour, animals were bilaterally implanted with LC optic fibre
614 stubs (fibre: 0.48 NA, 200-230 μm diameter, 6 mm length, Plexon) two-three weeks after viral
615 vector injection. Optic fibre tips were lowered to 100–200 μm above the CeA. Implants were fixed
616 to the skull with two miniature screws (00.90-100-M-SS-FH, US Micro Screw, Seattle, WA),
617 cyanoacrylate glue gel (SuperGlue, The original super glue, Ontario, CA) and dental cement
618 (Ortho-Jet powder and black liquid acrylate, Lang, Wheeling, IL). Experiments were conducted
619 four weeks after viral infections, to ensure adequate opsin expression.

620 *Lens implantation for Ca^{2+} Imaging*

621 Gradient index (GRIN) lens implantation surgery was performed as described previously.[46,47] Mice
622 were head fixed on the stereotaxic apparatus and a craniotomy was drilled over the DP
623 coordinates, using 1.2 mm diameter round drill burr (Harvard Apparatus, Holliston, MA). Three
624 additional holes were drilled to implant stainless steel screws (US Micro Screw, 00.90-100-M-SS-
625 FH). The skull surface was cleaned from bone fragments and wiped using sterilized cotton tips.
626 We aspirated the overlying tissue up to 1-1.5 mm above the site of implantation with a bent 27G
627 needle (NE-4527, Component supply, Sparta, TN) and performed intermittent sterile saline
628 washes to reduce intracranial pressure and improve the quality of the imaging site. A GRIN lens
629 (1 mm diameter, 9 mm length, 0.5 NA, 1 pitch, part # 1050-002177, Inscopix, Palo Alto, CA) was
630 attached to the stereotaxic arm using a custom-built lens holder, and lowered for 3 mm over the
631 course of 10 min. When the lens reached the required depth, Kwik-Sil (World Precision
632 Instruments, Sarasota, FL) was used to fill in the gap between the lens and the skull and left to
633 dry for 5 min. To hold the lens firmly in place, an adhesive cement (C&B S399 Metabond Quick
634 Adhesive Cement System Parkell, Edgewood, NY) mixed with liquid polymer (Catalyst + Quick
635 Base) was applied around the lens. After that, dental acrylic cement (Ortho-Jet powder and clear
636 liquid acrylate) was applied over the skull and screws and allowed to dry completely. The lens
637 holder was loosened and carefully detached from the lens. The layers of dental cement mixed

638 with black acrylate (Ortho-Jet powder and black liquid acrylate) were applied around the lens until
639 the height was ~0.5 mm below the top of the lens, and a thick layer of Kwik-cast (World Precision
640 Instruments, Sarasota, FL) was applied over the lens until it was embedded. This ridge around
641 the lens prevented lens damage during homecage activity and was used later for baseplate
642 implantation. Animals were then returned to the homecage, individually housed, and allowed to
643 recover for 2-3 weeks.

644 *Baseplating and verification of Ca^{2+} transients*

645 Mice were checked weekly for GCaMP6f fluorescence and Ca^{2+} transient activity over several
646 weeks after the lens implantation, as described before.[47] For baseplating, mice were anesthetized
647 with 5% isoflurane, fitted into the stereotaxic frame, and then maintained at 1%. A head-mounted
648 miniscope (V4, UCLA open-source, http://miniscope.org/) was fixed on a custom-built holder that
649 was attached to the stereotaxic arm.[48] The focusing mechanism of the miniscope was set at mid-
650 range to leave enough distance for focus adjustments in either direction. The coaxial cable from
651 the miniscope was attached to the data acquisition box (DAQ-V3.2, UCLA), which was connected
652 to the computer through USB 3.0. The baseplate was attached to the bottom of the miniscope.
653 We aligned the miniscope objective lens over the relay lens implanted in the mouse brain, and
654 the miniscope was moved to approach the relay lens. The recording software (Miniscope
655 controller, UCLA) was turned on and LED light intensity (25%), gain, and frame rate (30 fps) were
656 set. To ensure maximum field of view and focus on the centre of the lens, the miniscope tilt was
657 adjusted to view all edges of the relay lens. Then, the miniscope was slowly moved in X, Y, Z
658 planes to locate active cells/transients. If there were no transients, the mouse was returned to the
659 homecage and checked again the following week.

660 If Ca^{2+} transients were observed, they were further confirmed using tail pinch. If multiple cells
661 were observed, these mice were then considered for baseplating. After finding the optimal focal

662 plane and clear field of view, the baseplate was fixed on the mouse skull. Dental cement mixed
663 with black acrylate (Ortho-Jet powder and black liquid acrylate) was applied layer-by-layer
664 between the baseplate and the circular ridge built during lens implantation. The dental cement
665 was applied sufficiently so that no light could pass through from the outside. After the cement was
666 dry, the miniscope was detached and a plastic cover was installed to protect the relay lens.

667 **Miniscope recordings**

668 Animals with Ca^{2+} transients were used for behavioural experiments (N = 6). First, the mice were
669 subjected to preconditioning on day 1, and their behaviour as well as Ca^{2+} responses were
670 recorded. Animals were conditioned in the high-threat context for 2 days (5 trials/day, 0.9 mA
671 shock intensity), followed by recall in the low-threat context on day 4 (4 trials/day). The Ca^{2+}
672 response data was at 30 frames/sec rate. Behaviour was simultaneously recorded to video ("Pike"
673 camera, Allied vision, Germany). Neuronal recordings were started 10 s before the start of each
674 trial (at the onset of preSCS) and turned off 10 sec after the end of shock/ cue (post-shock/cue),
675 while behaviour was continuously recorded. Mice with flight responses only included in the for the
676 ca^{2+} data analysis.

677 **Ca^{2+} imaging processing.**

678 Ca^{2+} imaging videos were concatenated using ImageJ software
679 (https://imagej.nih.gov/ij/download.html). The concatenated videos were then processed using
680 MATLAB and an open source analysis package (https://bahanonu.github.io/ciatah/) as described
681 previously.[47,49] The videos were pre-processed by correcting for motion and temporally
682 downsampled by a factor of six. After pre-processing the videos, we extracted individual neurons
683 and their activity traces by using the open-source package Constrained Nonnegative Matrix
684 Factorization for microEndoscopic data (CNMF-E; https://github.com/zhoupc/CNMF-E). The

685 extracted cells were then manually identified based on the spatial filter and activity trace of each
686 candidate cell along with the candidate cells' average Ca^{2+} transient waveform. Data were
687 averaged over a 200 ms sliding window. The data was normalized by calculating Z-scores
688 (subtracting mean activity scores during all preSCS trials from each activity trace, divided by the
689 standard deviation of each cell during all preSCS trials) and the neurons with peaks that were ≥3
690 s.d. above baseline were considered as active neurons. To determine statistically significant
691 changes in responses of the DP-to-CeA projecting cells to the tone and WN, the Z-scores from
692 the corresponding periods were averaged and compared.

693 After finishing the experiments animals were perfused and their brains were isolated to confirm
694 the lens placements. The data from animals with correct lens placement was used for analysis.

695 **Behavioural paradigms**

696 *Conditioned flight paradigm*

697 Two different contexts were used. Context A (low-threat context) consisted of a clear cylindrical
698 chamber with a smooth floor, while Context B (high-threat context) consisted of a square
699 enclosure with an electrical grid floor used to deliver alternating current footshocks (ENV-414S,
700 Med Associates Inc., Fairfax, VT). These two chambers were cleaned with 1 % acetic acid and
701 70 % ethanol, respectively. A speaker (ENV-224AM, Med Associates Inc.) was mounted above
702 the chambers to deliver auditory stimuli at 75 dB. A programmable audio generator (ANL-926,
703 Med Associates, Inc.) generated auditory stimuli. Behavioural protocols were generated using
704 MedPC software (Med Associates, Inc.) to control auditory stimuli and footshock via TTL pulses.

705 We used a four-day paradigm as described previously.[2,21] On Day 1, animals were subjected to
706 pre-exposure in context A. After a 3 min baseline period, there were 4 presentations of a serial
707 compound stimulus (SCS, 20 s long) with a 90 s average pseudorandom intertrial interval (ITI)

708 (range 80−100 s). The SCS consisted of a 10 s tone (7.5 kHz, 500 ms pips at 1 Hz) and a 10 s
709 white noise (WN, random distribution of 1 to 20,000 Hz, 500 ms pips at 1 Hz). The total duration
710 of the pre-exposure session was 590 s. On Day 2 and Day 3 (conditioning days), mice were
711 placed in Context B and, after a 3 min baseline period, presented with five pairings of the SCS
712 with a 120 s average pseudorandom ITI (range 90−150 s) co-terminating with a 1 s, 0.9 mA
713 footshock (0.68 mA shock for ChR2 mediated stimulation groups). Each conditioning session
714 lasted for 820 s. Recall session on day 4 was conducted in Context A (or Context B for recall in
715 high-threat context group). Following a 3 min baseline period, mice were presented with 4 trials
716 of the SCS without footshock, with a 90 s average pseudorandom ITI (range 80−100 s) over a
717 total period of 590 s.

718 For optogenetic inhibition/control experiments the mice were presented with 8 trials on Day 3 with
719 4 pairs of alternating light ON-OFF trials (counter-balanced). During recall mice were presented
720 with 3 pairs of alternating light ON-OFF trials.

721 For rest of the optogenetic excitation/control experiments the mice were presented with 5 trials
722 on Day 3 with 2 pairs of alternating light ON-OFF trials (counter-balanced). During recall mice
723 were presented with 2 pairs of alternating light ON-OFF trials (counter-balanced). For recall
724 experiment in the high-threat context, we presented mice with 5 trials, all ON, for ChR2 and EYFP
725 controls.

726 *Quantification of defensive behaviour*

727 All sessions were recorded to video, and behaviour was analysed using contour tracking
728 (Cineplex software, Plexon, Dallas, TX). Freezing was defined as a complete cessation of
729 movement for at least 1 s and was automatically scored using a frame-by-frame analysis of pixel
730 changes (Cineplex Editor, Plexon). Results were confirmed by a trained observer blinded to

731 condition. By determining a calibration coefficient using the chambers' known size and the
732 camera's pixel dimensions, speed (cm/s) was extracted using the animal's centre of gravity.[21]
733
734 Escape jumping was scored manually from video files by a blinded observer. Flight scores were
735 calculated by dividing the average speed during each CS by the average speed during the 10 s
736 pre-CS from all the trials (baseline, BL) and then adding 1 point for each escape jump (speedCS/
737 speedBL + # of jumps). A flight score of 1 therefore indicated no change in flight behaviour from
738 the preSCS period.

739 *Open field test*

740 A 45 x 45 x 45 cm arena made of white opaque Plexiglas was used. The arena was cleaned using
741 70% ethanol after each mouse. Mouse behaviour was tracked under 100 lux light conditions using
742 a top-mounted camera ("Pike" camera, Allied vision, Germany).
743 *For chemogenetic* experiments, the OFT duration was 10 min.
744 *For optogenetic experiments*, the OFT duration was 6 min. After a 120 s baseline period, 4, 30
745 sec ON-OFF trials of light stimulation were used. For eNpHR experiments, a continuous orange
746 light was used at 10 mW power at the fibre tip, and for ChR2 experiments, 10 ms pulses of blue
747 light were used at 10 Hz, and 10 mW power at the fibre tip.
748 The time spent in the inner zone, the number of entries into it, and total distance traveled were
749 measured using tracking software (Cineplex Studio, Plexon).
750

751 *Elevated plus maze*

752 Behaviour was tracked using a top-mounted camera ("Pike" camera, Allied vision, Germany) for
753 10 min. The maze was made from white opaque Plexiglas material and consisted of four 30 cm
754 long and 7 cm wide arms. Two open arms had no walls, and two enclosed arms had 15 cm high
755 walls. The maze was elevated 40 cm above the ground. The arena was cleaned using 70%

756 ethanol after every test. The total time spent in the open arms was calculated using Cineplex
757 Editor software (Plexon).
758
759 **Chemogenetic manipulations of behaviour**
760 Behavioural testing was performed 3-4 weeks after viral injections. First, mice were subjected to
761 the OFT. On the next day, animals were subjected to the EPM. Thirty min before the start of
762 behavioural testing animals were injected with clozapine N-oxide [CNO; 0.5 mg/ml in vehicle
763 (0.9% saline), given as 10 ml/kg for final dose of 5 mg/kg, intraperitoneally (ip); Enzo Life
764 Sciences, Farmingdale, NY] or vehicle (10 ml/kg volume, ip).
765
766 **Optogenetic manipulations of behaviour**
767 Two-three weeks after vector injection, animals were implanted with fibre stubs (Plexon) targeting
768 CeA, as described in Surgery. For optogenetic modulation, we used a Plex controller system
769 (Plexon) operated through Radiant software (Plexon). Two PlexBright LED modules (Plexon)
770 were connected to the controller, and an LC patch cable (200-230 μm fibre, 1 meter long, 0.66
771 NA, Plexon) was connected. Laser power at the fibre tip was measured before every test with an
772 optical power and energy meter (PM100D, ThorLabs, Newton, NJ). The patch cable was
773 connected to the head-mounted fibre stubs using ceramic sleeves. Connectors were tested for
774 coupling efficiency before implantations, and laser power at the fibre tip for behavioural
775 manipulations was adjusted to reach a value of 10 mW.
776
777 Experiments were performed with a within-subjects design in which mice underwent eight trials
778 (5 trials for ChR2 groups) during FC2 with alternating 2-2 trials of LED ON-OFF. During recall
779 session, mice underwent six trials (4 trials for ChR2 groups) with alternating light on off conditions.
780 To inhibit (eNpHR) DP-CeA neuronal populations during threat cues, a 620 nm light was switched

781 on 500 ms before the onset of the SCS (first tone pip) and remained on until the end of the last
782 white noise pip or (20.5 s in total).
783 For ChR2-induced excitation (0.9 mA footshock intensity group) of DP-to-CeA neuronal
784 populations, we used 465 nm light pulses (10 Hz, 10 ms width) which was switched on 500 ms
785 before the onset of the SCS (first tone pip) and remained on until the end of the last white noise
786 pip (20.5 s in total).
787 In addition, for ChR2 manipulation during low footshock intensity (0.68 mA) groups, the 465 nm
788 light pulses (10 Hz, 10 ms width) were delivered when first WN pip was on and remained on until
789 the end of 10 sec post cue periods (20.5 s in total).

790 **Real-time place aversion test**

791 To test whether optogenetic stimulation of the DP-to-CeA pathway induced aversive responses,
792 we subjected the AAV-DIO-ChR2-EYFP or AAV-DIO-EYFP-injected mice to real-time place
793 aversion test for 10 min. We used a custom-made 50 × 50 × 50 cm arena made from white opaque
794 Plexiglas and divided into two equal compartments. One side of the chamber was allotted as the
795 stimulation side and other as a neutral side (non-stimulated, with striped walls and metallic plate
796 floor). Mice were placed in the non-stimulated side, and 10 Hz blue LED light stimulation was
797 delivered each time the mouse moved to the stimulation side of the chamber. The light stimulation
798 was continuously on until the mouse moved back into the non-stimulation compartment.
799 Behaviour was recorded via a top mounted recording camera attached to recording system
800 (Plexon) and scored using Cineplex editor (Plexon) by a blinded experimenter. The % time spent
801 in the stimulation chamber was used as a measure of aversion.
802

803 **Immunohistochemistry (IHC)**

804 Following the completion of experiments, mice were anesthetized with tribromoethanol (240
805 mg/kg) and perfused transcardially with phosphate-buffered saline (PBS) followed by 4%

806 paraformaldehyde in PBS. Brains were isolated and stored in paraformaldehyde overnight. On
807 the next day, fixed brains were sectioned using a vibrating microtome (Precisionary, Greenville,
808 NC) in 60- (for cFos IHC) or 80-µm thick coronal slices.
809
810 Antibody staining was performed on floating tissue sections. Briefly, sections were washed in
811 PBS-TritonX100 (PBST, 0.3%) and blocked using 5% goat serum in PBST for 1 hr followed by an
812 overnight (for RFP or GFP staining), or 48-h (for cFos staining), incubation in primary antibodies
813 at 4°C. Primary antibodies used in this study were rabbit anti-RFP (1:1500, 600-401-379,
814 Rockland Immunochemicals, Pottstown, PA), chicken anti-GFP (1:2000, NB100-1614, Novus
815 Biologicals, USA), rabbit anti-cFos (1:1000, 226003, Synaptic Systems, Germany). After primary
816 antibody incubation, sections were washed in PBST and incubated in secondary antibodies in
817 PBST (1:500 goat anti-rabbit AlexaFluor 555/488 or goat anti-chicken AlexaFluor 488, Thermo
818 Fisher Scientific, USA). Following final rinses with PBS, sections were mounted and scanned from
819 the DP and CeA.
820 Images were obtained using an Axio Scan.Z1 slide-scanning microscope (Zeiss, Germany) and
821 a confocal microscope (FV3000, Olympus, Japan). Mice were included in subsequent data
822 analyses only if bilateral expression specific to the target region was observed.

823 **cFos quantification**

824 Red fluorescent retro-beads were injected into the CeA of C57BL/6J mice. 7 days later, animals
825 were divided into 4 groups: homecage control, shock-only, SCS-FC and unpaired. Shock-only,
826 unpaired and SCS-FC mice were subjected to two days of conditioning and were sacrificed 90
827 min after the second session by transcardial perfusion. Following brain sectioning and IHC
828 staining for cFos, confocal images were taken. The quantification of cFos+, bead+, and cells with
829 both markers were performed by a blinded observer using ImageJ.
830

831 **Brain slice electrophysiology**

832 *Slice preparation:* Coronal brain slices containing the CeA were collected from mice at least two
833 weeks after viral injections for *ex vivo* electrophysiological recordings, as described earlier.[38,50]
834 Mice (9+ weeks) were decapitated in a restraining plastic cone (DecapiCone, Braintree Scientific,
835 Braintree, MA) and the brains were dissected and immersed in ice-cold, oxygenated cutting
836 solution containing the following (in mM): 252 sucrose, 2.5 KCl, 26 $NaHCO_3$, 1 $CaCl_2$, 5 $MgCl_2$,
837 1.25 NaH_2PO_4, 10 glucose. The brains were trimmed and glued to the chuck of a Leica VT-1200
838 vibratome (Leica Microsystems, Germany) and 300 µm-thick coronal slices were sectioned.
839 Slices were transferred to a holding chamber containing oxygenated recording artificial
840 cerebrospinal fluid (aCSF) containing (in mM): 126 NaCl, 2.5 KCl, 1.25 NaH_2PO_4, 1.3 $MgCl_2$, 2.5
841 $CaCl_2$, 26 $NaHCO_3$, and 10 glucose. They were maintained in the holding chamber at 34°C for 30
842 min before decreasing the chamber temperature to ~20°C.

843

844 *Patch clamp recording:* Slices were bisected down the midline and hemi-slices were transferred
845 from the holding chamber to a submerged recording chamber mounted on the fixed stage of an
846 Olympus BX51WI fluorescence microscope equipped with differential interference contrast (DIC)
847 illumination. The slices in the recording chamber were continuously perfused at a rate of 2 ml/min
848 with recording aCSF maintained at 32-34°C and continuously aerated with 95% O_2/5% CO_2.
849 Whole-cell patch clamp recordings were performed in eYFP-labeled SOM+ or CRH+ neurons,
850 retrolabeled neurons (beads from dl/l or vl PAG), or unlabeled neurons in the CeM or CeL. Glass
851 pipettes with a resistance of 3-5 MΩ were pulled from borosilicate glass (ID 1.2mm, OD 1.65mm)
852 on a horizontal puller (Sutter P-97) and filled with an intracellular patch solution containing (in
853 mM): 130 potassium gluconate, 10 HEPES, 10 phosphocreatine Na_2, 4 Mg-ATP, 0.4 Na-GTP, 5
854 KCl, 0.6 EGTA; pH was adjusted to 7.25 with KOH and the solution had a final osmolarity of ~
855 290 mOsm. DNQX (20 uM) was delivered via the perfusion bath. Series resistance was normally
856 below 15 MΩ immediately after break-in and was continuously monitored. Cells were discarded

857 when the series resistance exceeded 30 MΩ. An optical fibre was placed approximately 2 mm
858 above the slice and ChR2-expressing DP fibres were stimulated by 465 nm LED illumination
859 (single 10-ms pulses,15 mW power, delivered at 1 Hz).
860 To assess firing properties in CeA neurons that displayed fast synaptic responses, 500-750 ms
861 depolarizing current injections were applied in current clamp mode. To compare the properties of
862 monosynaptic EPSCs evoked by optogenetic stimulation of DP fibers, responses were recorded
863 in the presence of 1 mM 4-aminopyridine and 1 uM tetrodotoxin. Data were acquired using a
864 Multiclamp 700B amplifier, a Digidata 1440A analog/digital interface, and pClamp 10 software
865 (Molecular Devices, San Jose, CA). Recordings were filtered at 4 KHz and sampled at 50 KHZ.
866 Data were analyzed with Clampfit 10 (Molecular Devices, San Jose, CA). Statistical comparisons
867 were conducted with a paired or unpaired Students's *t* test ($p < 0.05$ with a two- tailed analysis
868 was considered significant).
869

870 **Statistical analysis**

871 Data were analysed for statistical significance using Prism 10 (GraphPad Software, San Diego,
872 CA). Statistical significance was set at $p < 0.05$. Data were tested for normal distribution using the
873 Shapiro-Wilk normality test ($\alpha=0.05$). For pairwise comparisons, the appropriate parametric
874 (unpaired Student's t-test) or nonparametric (Mann-Whitney test) test was performed. Data with
875 more than two study groups were analysed using one-way ANOVA followed by Bonferroni's post-
876 hoc tests. For calcium imaging data analysis, we used custom code written in MATLAB.
877 Correlations analysis and plotting regression lines were performed using the GraphPad Prism 10.
878 The sample size was determined based on previously published research.
879

880 **Methods References**

881 45. Soudais, C., Laplace-Builhe, C., Kissa, K. & Kremer, E. J. Preferential transduction of
882 neurons by canine adenovirus vectors and their efficient retrograde transport in vivo.

883 *FASEB J.* **15**, 2283–2285 (2001).
884 46. Resendez, S. L. *et al.* Visualization of cortical, subcortical and deep brain neural circuit
885 dynamics during naturalistic mammalian behavior with head-mounted microscopes and
886 chronically implanted lenses. *Nat. Protoc.* **11**, 566–597 (2016).
887 47. Corder, G. *et al.* An amygdalar neural ensemble that encodes the unpleasantness of
888 pain. *Science* **363**, 276–281 (2019).
889 48. Ghosh, K. K. *et al.* Miniaturized integration of a fluorescence microscope. *Nat. Methods* **8**,
890 871–878 (2011).
891 49. Parker, J. G. *et al.* Diametric neural ensemble dynamics in parkinsonian and dyskinetic
892 states. *Nature* **557**, 177-182 (2018).
893 50. Chen, C. *et al.* Astrocytes amplify neuronal dendritic volume transmission stimulated by
894 norepinephrine. *Cell Rep.* **29**, 4349-4361.e4 (2019).
895

896 **Acknowledgements**

897 We thank Dr. Biafra Ahanonu (University of California, San Francisco) for providing MATLAB
898 codes and assistance with calcium imaging data analysis. We thank Dr. Ricardo Mostany (Tulane
899 University, New Orleans) and Dr. Seongsik Yun (Northwestern University, Chicago) for help in
900 standardization of calcium imaging and data analysis. This work was supported by the Louisiana
901 Board of Regents through the Board of Regents support fund (**LEQSF(2018-21)-RD-A-17**)
902 and *the National Institute of Mental Health* of the National Institutes of Health under award
903 number **R01MH122561**. The content is solely the responsibility of the authors and does not
904 necessarily represent the official views of the National Institutes of Health.
905

906 **Author contributions:**

Conceptualization— CDB, JPF; Formal analysis— CDB, CS, XF, MD, QEL, RV, CV, AW, SB, AD, EB, AR, JP, JPF; Funding acquisition— JPF; Investigation— CDB, CS, XF, QEL; Methodology— CDB, MD, CS, JT, JPF; Project Administration / Supervision— CDB, JPF, JT Resources— JPF, JT; Visualization— CDB, CS, MD, XF, JPF; Writing, original draft— CDB, JPF; Writing, review & editing— CDB, CS, XF, JT, JP, JPF

Competing Interest Statement

The authors declare no competing interests.

Additional Information

Correspondence and requests for materials should be addressed to JPF.

Data availability

Data sets included in this study are available from the corresponding author upon reasonable request.

Extended Data

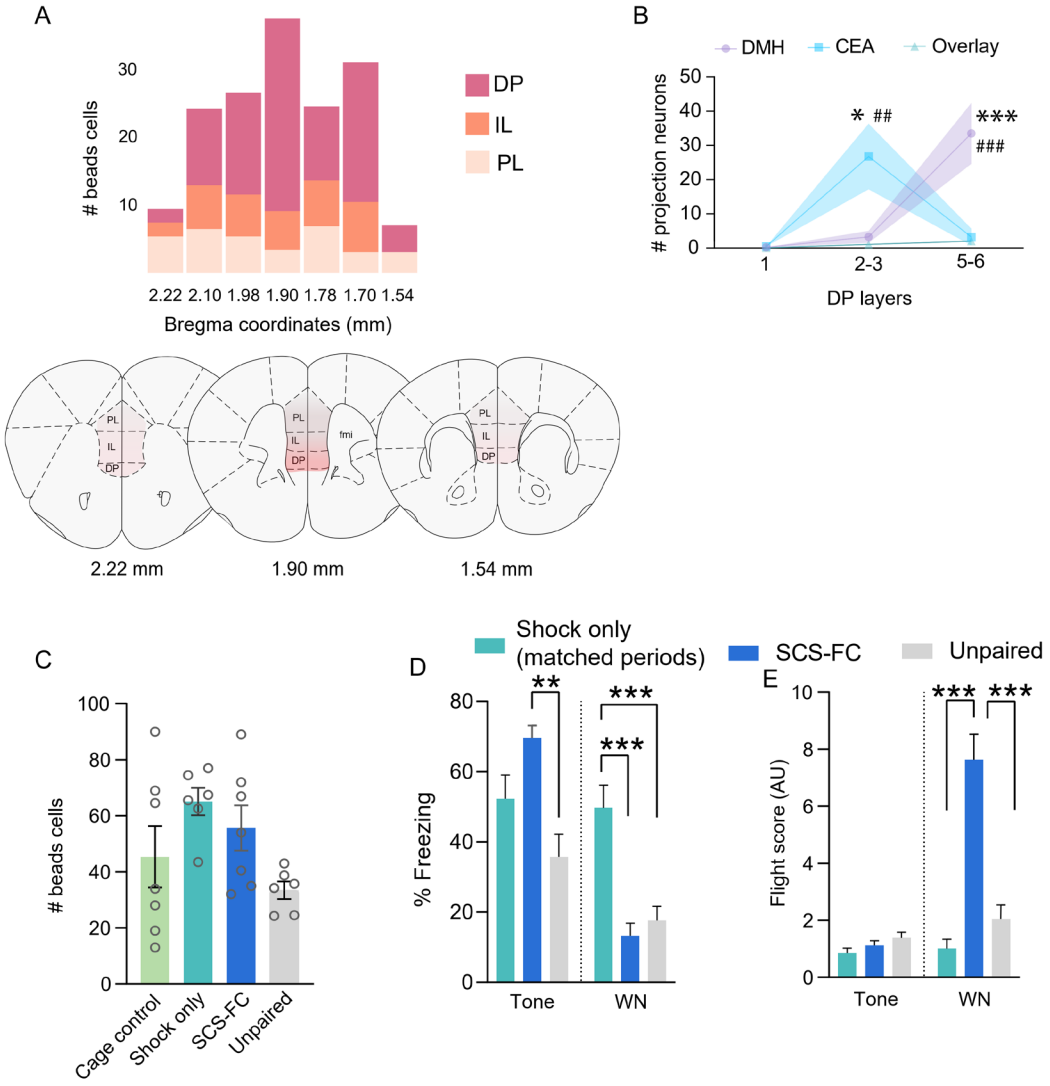

Figure S1(Data related to Figure 1): Neuroanatomy of the DP-CeA pathway

A, *Top,* Number of CeA-projecting mPFC cells across the antero-posterior axis (2.22 mm to 1.54 mm). *Bottom,* Schematic of coronal sections showing the density of beads in DP on anterio-posterior scale.

B, The layer-wise distribution of bead+ cells in the DP that project to CeA and/or DMH (N = 6; Two-way ANOVA, layer x group, $F_{(4, 45)} = 10.15$, $p < 0.0001$, followed by Bonferroni's post-hoc test). *$p<0.05$, *** $p<0.001$ (DMH vs CeA), $^{\#\#}p<0.01$, $^{\#\#\#}p<0.001$ (vs overlay).

931 **C**, Total number of bead+ cells across groups (N = 6; 3-4 slices per group). One-way ANOVA,

932 $F_{(3, 22)} = 2.819$, $p = 0.0626$.

933 **D**, Freezing of cFos groups on FC2. One-way ANOVA for tone $F_{(2, 15)} = 8.502$, $p = 0.0034$ and

934 white noise (WN; $F_{(2, 15)} = 18.43$, $p < 0.0001$), followed by Bonferroni's post-hoc test. **$p < 0.01$,

935 *** $p < 0.001$.

936 **E**, Flight scores of cFos groups on FC2. One-way ANOVA for tone ($F_{(2, 15)} = 1.87$, $p = 0.18$) and

937 white noise (WN) $F_{(2, 15)} = 33.11$, $p < 0.0001$, followed by Bonferroni's post-hoc test. *** p

938 < 0.001.

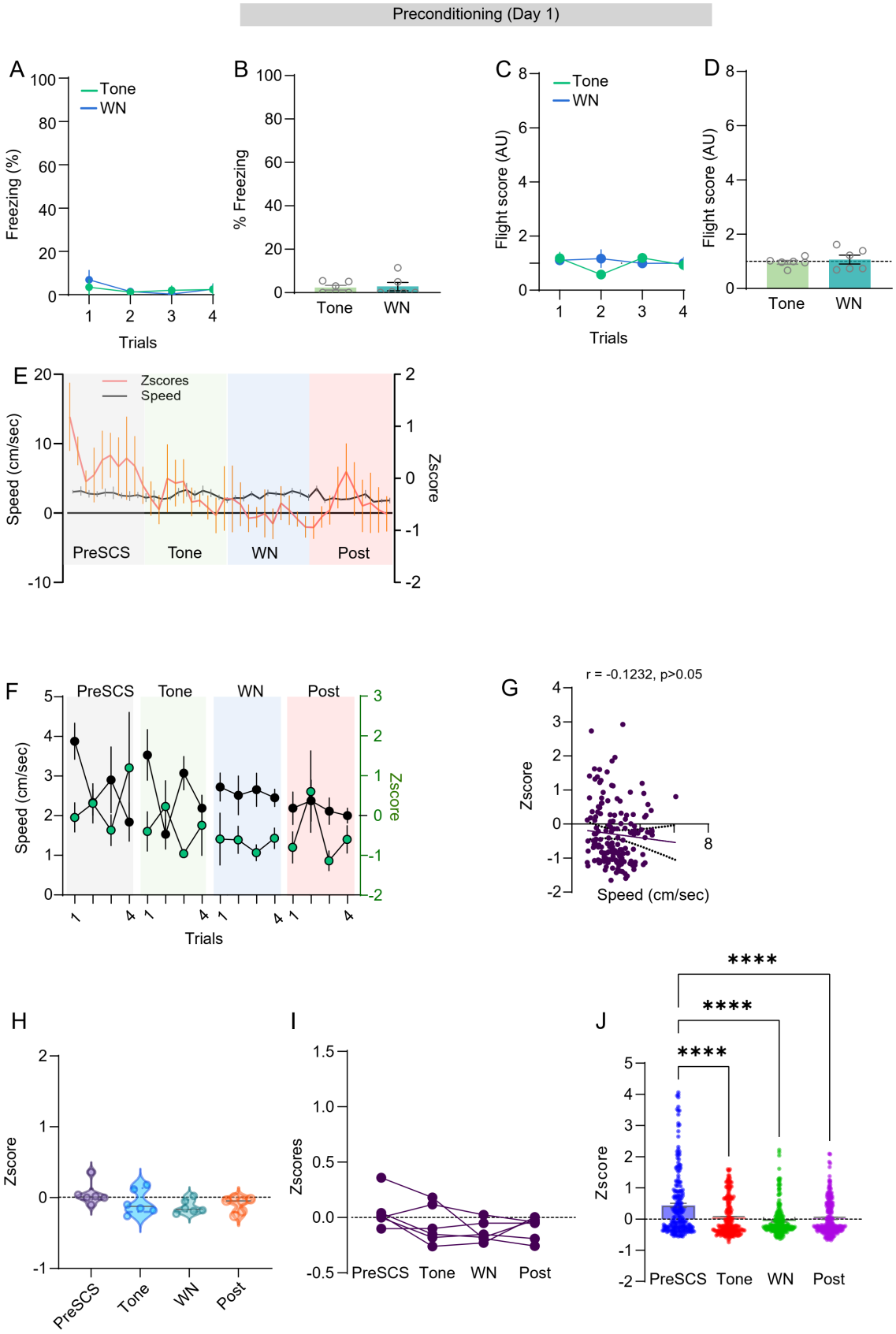
Preconditioning (Day 1)
A
Freezing (%)
Tone
WN
Trials
B
% Freezing
Tone
WN
C
Flight score (AU)
Tone
WN
Trials
D
Flight score (AU)
Tone
WN
E
Speed (cm/sec)
Zscores
Speed
Zscore
PreSCS
Tone
WN
Post
F
PreSCS
Tone
WN
Post
Speed (cm/sec)
Zscore
Trials
G
r = -0.1232, p>0.05
Zscore
Speed (cm/sec)
H
Zscore
PreSCS
Tone
WN
Post
I
Zscores
PreSCS
Tone
WN
Post
J
****
****
****
Zscore
PreSCS
Tone
WN
Post

939

940 **Figure S2 (Data related to Figure 2): Calcium imaging during pre-conditioning**

941 **A-B**, Trial-wise and cumulative freezing of mice from calcium imaging experiments during
942 preconditioning session (N = 6, Paired t-test, t=0.3051, df=5, p = 0.77).

943 **C-D**, Trial-wise and cumulative flight score of mice from calcium imaging experiments during
944 preconditioning session (N = 6, Paired t-test, t=0.6565, df=5, p = 0.54).

945 **E**, Speed and neuronal activity during the last trial of preconditioning session (Day 1, n = 221)).

946 **F**, Average speed and neuronal activity during each trial of preSCS, tone, WN and post-cue
947 periods.

948 **G**, Correlation of speed and neuronal activity from all trials (10 sec each epoch of preSCS, tone,
949 WN and post cue, each point represents one sec). Spearman correlation, r = -0.1232, 95% CI: -
950 0.2774 to 0.03724, p >0.05.

951 **H**, Average Z-score of the DP-to-CeA population during the preSCS, tone, WN and post-cue
952 periods (Ordinary one-way ANOVA, $F_{(3, 20)} = 1.965$, p = 0.15).

953 **I**, Average Z-scores of individual mice during preSCS, tone, WN and post-cue periods (N = 6).

954 J, Z-scores of individual neurons during the last trial of preconditioning (N = 6, total neurons =
955 221, One-way ANOVA, $F_{(3, 880)} = 21.43$, P<0.0001, followed by Bonferroni's multiple
956 comparisons test, ****p<0.0001)

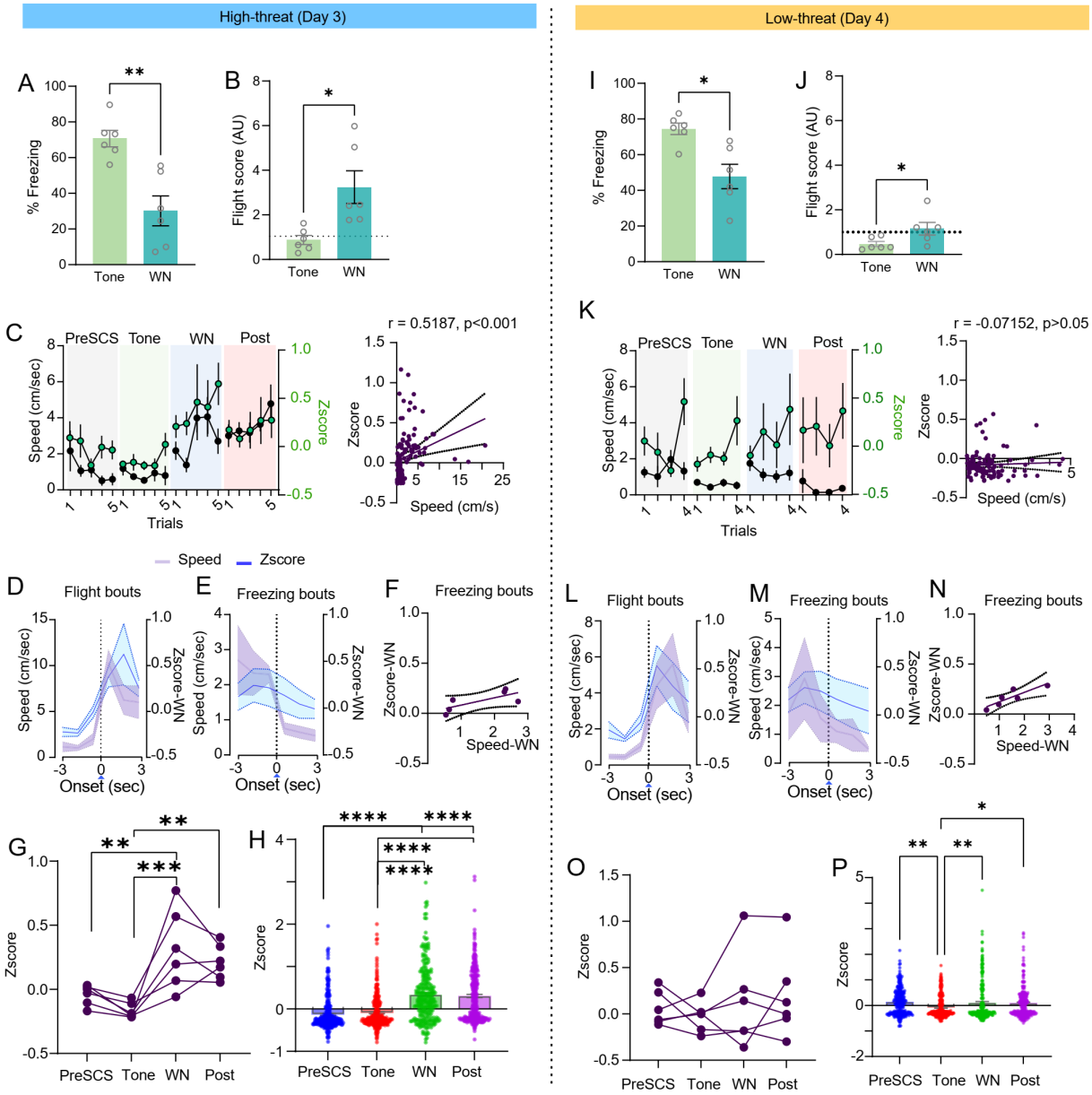

Figure S3 (Data related to Figure 2): Calcium imaging in the high-threat and low-threat contexts.

A, Freezing behaviour in the high-threat context (N = 6). Paired t-test, t=4.744, df=5, $^{**}p < 0.01$.

B, Flight scores in the high-threat context (N = 6). Paired t-test, t=3.650, df=5, $^{*}p < 0.05$.

C, *left*, Average speed and neuronal activity during each trial of the preSCS, tone, WN and post-cue periods in the high-threat context (n = 273). Data shown as means ± s.e.m. *right*,

964 Correlation of speed and neuronal activity from the last 3 trials (preSCS, tone, WN and post-cue
965 epochs, each point represents data from 1 sec). Spearman correlation, r = 0.5187, 95% CI:
966 0.3696 to 0.6417, p<0.001.
967 **D**, Speed and neuronal activity aligned to the onset of flight bouts during WN in the high-threat
968 context. Data shown as means ± s.e.m.
969 **E**, Speed and neuronal activity aligned to the onset of freezing bouts during WN in the high-
970 threat context. Data shown as means ± s.e.m.
971 **F**, Spearman correlation plot for speed and Z-score from the identified freezing bouts (each dot
972 represents values at each sec of the bouts, r = 0.657, 95% CI = -0.02019 to 0.1662, p = 0.175).
973 **G**, The linegraph showing the Z-scores of individual mice during preSCS, tone, WN and post-
974 cue periods, across all trials (N = 6, One-way ANOVA, $F_{(3, 20)}$ = 9.331, P=0.0005, followed by
975 Bonferroni's multiple comparisons test. *p < 0.05, **p < 0.01, ***p < 0.001).
976 **H**, The Z-scores of individual neurons during preSCS, tone, WN and post-cue periods, from the
977 last trial in the high-threat context (N = 6, total neurons = 273, One-way ANOVA, $F_{(3, 1112)}$ =
978 59.01, P<0.0001, followed by Bonferroni's multiple comparisons test, ****p < 0.0001).
979 **I**, Freezing in the low-threat context (N = 6). Paired t-test, t=3.424, df=5, *p < 0.05.
980 **J**, Flight scores in the low-threat context (N = 6). Paired t-test, t=2.889, df=5, *p < 0.05.
981 **K**, *left*, Change in average speed and neuronal activity during preSCS, tone, WN and post-cue
982 periods in the low-threat context (Day 4) over 4 trials (n = 253). Data shown as means ± s.e.m.
983 *right*, Correlation of speed and neuronal activity from all recall trials in the low-threat context
984 (preSCS, tone, WN and post cue epochs, each point represents 1 sec of data). Spearman
985 correlation, r = -0.07152, 95% CI: -0.2526 to 0.1144, p>0.05.
986 **L**, Speed and neuronal activity aligned to the onset of flight bouts during WN in the low-threat
987 context. Data shown as means ± s.e.m.
988 **M**, Speed and neuronal activity aligned to the onset of freezing bouts during WN in the low-
989 threat context. Data shown as means ± s.e.m.

N, Spearman correlation of speed and neuronal activity from freezing bouts (each point represents one sec of data, r = 0.82, 95% CI = 0.02337 to 0.1669, P = 0.058).

O, Population activity of individual mice during preSCS, tone, WN and post-cue periods, across all trials (N = 6, One-way ANOVA, $F_{(3,20)} = 0.3923$, $P = 0.75$, followed by Bonferroni's multiple comparisons test).

P, Neuronal activity of individual neurons during preSCS, tone, WN and post-cue periods, from the last trial in the low-threat context (N = 6, total neurons = 253, One-way ANOVA, $F_{(3,1008)} = 5.566$, $P = 0.0009$, followed by Bonferroni's multiple comparisons test, $^{*}p < 0.05$, $^{**}p < 0.01$).

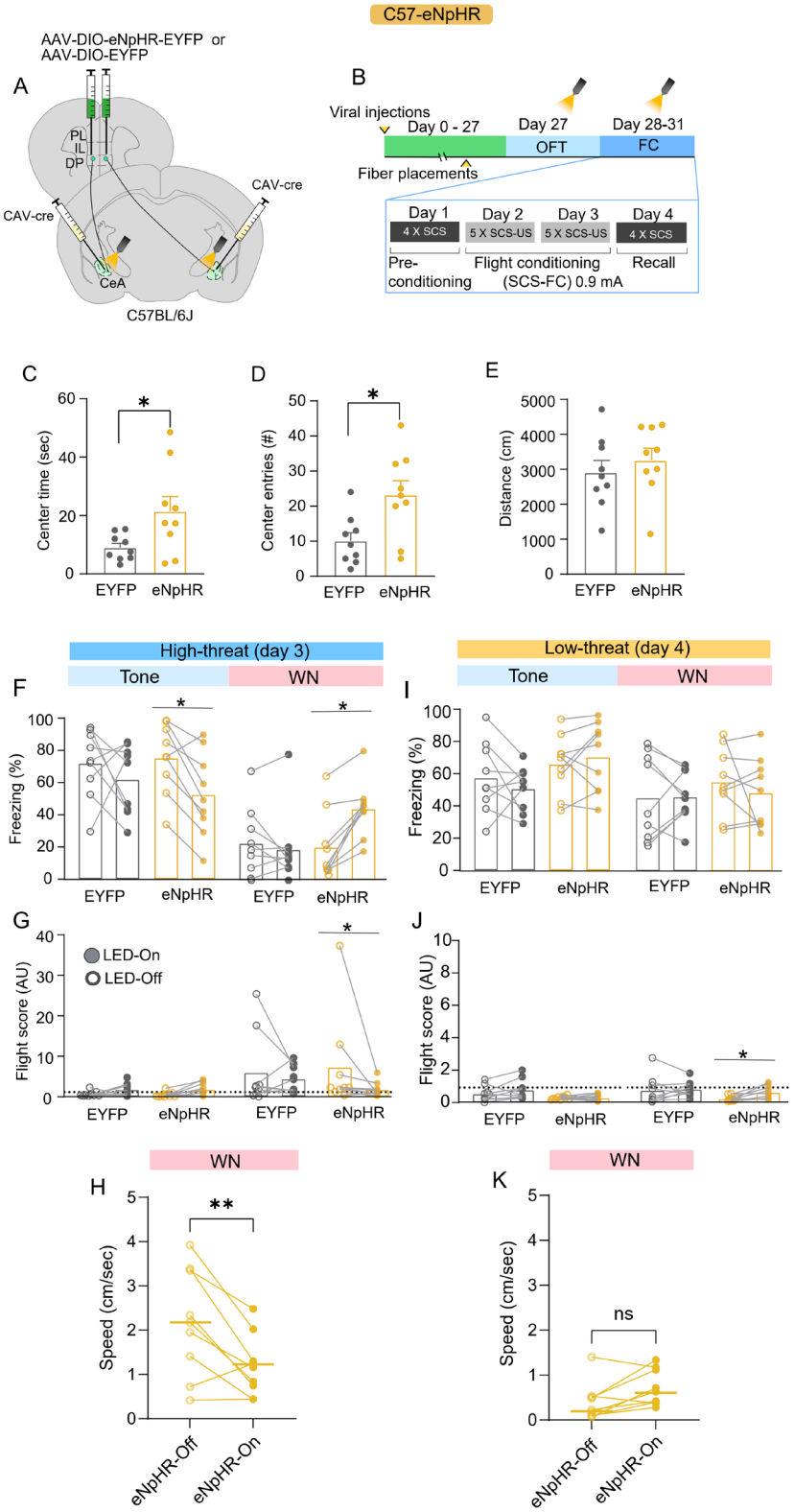

Figure S4 (Data related figure 4): Optogenetic inhibition of the DP-CEA pathway

1000 **A**, Intersectional approach used for optogenetic terminal inhibition of the DP-to-CeA neuronal
1001 projections.
1002 **B**, Experimental timeline.
1003 **C-E**, Effect of optogenetic inhibition on centre time (**C**), centre entries (**D**), and distance travelled
1004 (**E**) in OFT in EYFP (N = 9) and eNpHR (N = 9) groups. Unpaired t-test, *$p < 0.05$.
1005 **F**, Effect of optogenetic inhibition in EYFP (N = 9) and eNpHR (N = 9) groups on freezing in the
1006 high-threat context (LED-on vs LED-off, Mann-Whitney, *P<0.05).
1007 **G**, Effect of optogenetic inhibition in EYFP (N = 9) and eNpHR (N = 9) groups on flight in the
1008 high-threat context (LED-on vs LED-off, Mann-Whitney, *P<0.05).
1009 **H**, Effects of optogenetic inhibition on speed in the high-threat context during WN in the eNpHR
1010 group (N = 9; Paired t-test t=3.497, df=8, p = 0.0081).
1011 **I**, Effect of optogenetic inhibition in EYFP (N = 9) and eNpHR (N = 9) groups on freezing in the
1012 low-threat context (LED-on vs LED-off, Mann-Whitney, n.s.).
1013 **J**, Effect of optogenetic inhibition in EYFP (N = 9) and eNpHR (N = 9) groups on flight in the
1014 low-threat context (LED-on vs LED-off, Mann-Whitney, *P<0.05).
1015 **K**, Effect of optogenetic inhibition on speed in the low-threat context during WN in the eNpHR
1016 group (N = 9; paired t-test,t=2.619, df=8, p = 0.307).

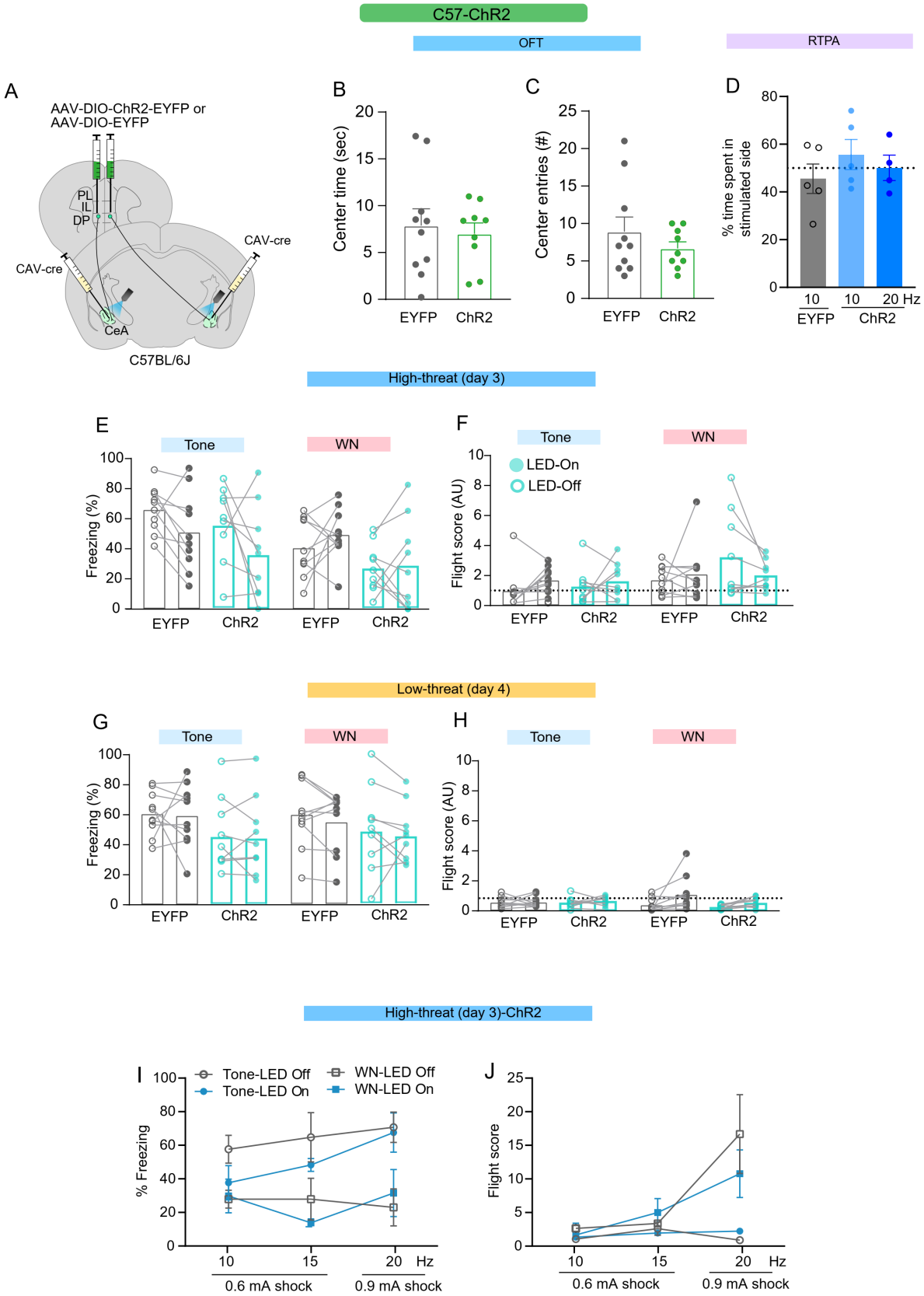
C57-ChR2
OFT
RTPA
A
AAV-DIO-ChR2-EYFP or
AAV-DIO-EYFP
PL
IL
DP
CAV-cre
CAV-cre
CeA
C57BL/6J
B
Center time (sec)
EYFP
ChR2
C
Center entries (#)
EYFP
ChR2
D
% time spent in stimulated side
10
10
20 Hz
EYFP
ChR2
High-threat (day 3)
E
Tone
WN
Freezing (%)
EYFP
ChR2
EYFP
ChR2
F
Tone
WN
LED-On
LED-Off
Flight score (AU)
EYFP
ChR2
EYFP
ChR2
Low-threat (day 4)
G
Tone
WN
Freezing (%)
EYFP
ChR2
EYFP
ChR2
H
Tone
WN
Flight score (AU)
EYFP
ChR2
EYFP
ChR2
High-threat (day 3)-ChR2
I
Tone-LED Off
Tone-LED On
WN-LED Off
WN-LED On
% Freezing
10
15
20
Hz
0.6 mA shock
0.9 mA shock
J
Flight score
10
15
20
Hz
0.6 mA shock
0.9 mA shock

1017

1018 **Figure S5 (Data related figure 4): Non-cell type specific stimulation of the DP-CEA**
1019 **pathway**

1020 **A,** Intersectional approach used to target optogenetic stimulation to DP-to-CeA terminals.

1021 **B-C**, Effect of optogenetic stimulation on OFT centre time (**B**) and centre entries (**C**) in EYFP (N
1022 = 10) and ChR2 (N = 9) groups (Unpaired t-test, n.s.).

1023 **D**, Effects of optogenetic stimulation on real-time place avoidance in EYFP (10 Hz, N = 5) and
1024 ChR2 (10 Hz, N = 5; 20 Hz, N = 4) groups (One-way ANOVA ($F_{(2, 11)} = 0.73$, $p = 0.502$).

1025 **E**, Effect of optogenetic excitation in EYFP (N = 10) and ChR2 (N = 9) groups on freezing in the
1026 high-threat context (LED-on vs LED-off, Mann-Whitney, n.s.).

1027 **F**, Effect of optogenetic excitation in EYFP (N = 10) and ChR2 (N = 9) groups on flight in the
1028 high-threat context (LED-on vs LED-off, Mann-Whitney, n.s.).

1029 **G**, Effect of optogenetic excitation in EYFP (N = 10) and ChR2 (N = 9) groups on freezing in the
1030 low-threat context (LED-on vs LED-off, Mann-Whitney, n.s.).

1031 **H**, Effect of optogenetic excitation in EYFP (N = 10) and ChR2 (N = 9) groups on flight in the
1032 low-threat context (LED-on vs LED-off, Mann-Whitney, n.s.).

1033 **I-J**, Freezing (**I**) and flight scores (**J**) during optogenetic stimulation during day 3 at different
1034 stimulation frequencies and shock intensities (at 0.6 mA - 10 Hz, N = 9; 15 Hz, N = 3; at 0.9 mA
1035 - 20 Hz, N = 5). Two-way ANOVA (*for % freezing*, Stimulation frequency x Shock intensity, $F_{(6,}$
1036 $_{56)} = 0.76$, $p = 0.601$, Stimulation frequency, $F_{(2, 56)} = 1.10$, $p = 0.339$, Shock intensity, $F_{(3, 56)} =$
1037 8.37, $p = 0.0001$; *for flight*, Stimulation frequency x Shock intensity, $F_{(6, 56)} = 4.42$, $p = 0.001$,
1038 Shock intensity, $F_{(3, 56)} = 6.66$, $p = 0.001$, followed by Bonferroni's post hoc test (tone/WN ON vs
1039 OFF non-significant).

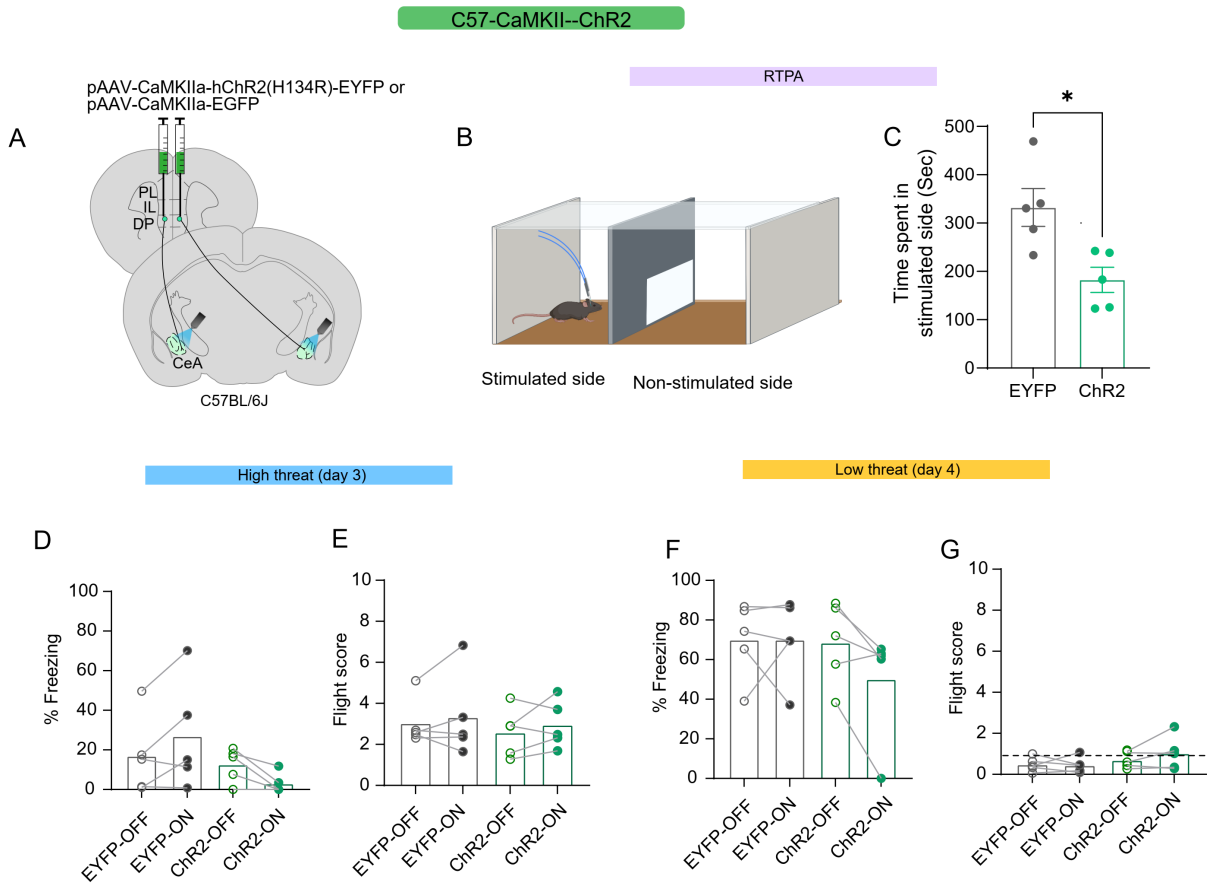

Figure S6 (Data related figure 4): Stimulation of theDP-CEA pathway using a CaMKII promotor

A, Viral injection strategy for optogenetic terminal stimulation of DP-to-CeA neuronal projections.

B-C, Schematic (**B**) and results of real-time place aversion (RTPA) in EYFP (20 Hz, N = 5) and ChR2 (20 Hz, N = 5) groups. Unpaired t-test, t=3.191, df=8, *P <0.05.

D, Effect of optogenetic excitation in EYFP (N = 5) and ChR2 (N = 5) groups on freezing in the high-threat context (LED-on vs LED-off, paired t-test, n.s.).

E, Effect of optogenetic excitation in EYFP (N = 5) and ChR2 (N = 5) groups on flight scores in the high-threat context (LED-on vs LED-off, paired t-test, n.s.).

F, Effect of optogenetic excitation in EYFP (N = 5) and ChR2 (N = 5) groups on freezing in the low-threat context (LED-on vs LED-off, paired t-test, n.s.).

1053 **G**, Effect of optogenetic excitation in EYFP (N = 5) and ChR2 (N = 5) groups on flight scores in

1054 the low-threat context (LED-on vs LED-off, paired t-test, n.s.).

1055

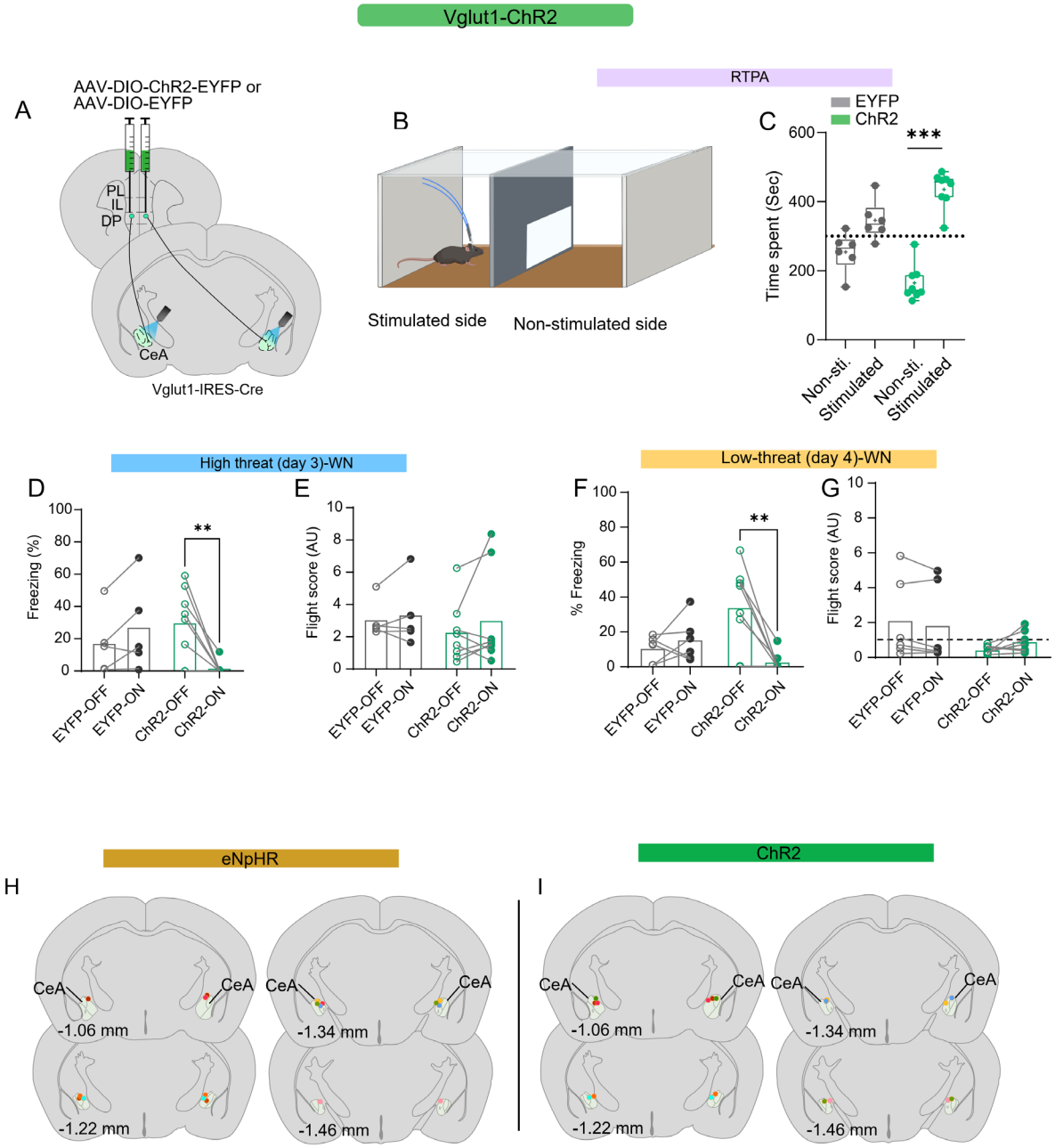

Figure S7 (Data related figure 4): Optogenetic stimulation of the DP-CEA pathway in Vglut1 mice

A, Viral injection strategy for optogenetic terminal stimulation of DP-to-CeA neuronal projections.

1061 **B-C**, Schematic (**B**) and real-time place aversion (RTPA) performance (**C**) from EYFP (N=6)
1062 and ChR2 (N=8) groups (unpaired t-test, EYFP (t=1.974, df=5, P =0.10), ChR2 (t=7.339, df=7,
1063 ***P =0.0002).

1064 **D**, Effect of optogenetic excitation in EYFP (N = 6) and ChR2 (N = 8) groups on freezing during
1065 WN in the high-threat context (LED-on vs LED-off, Paired t-test, ChR2, t=3.650, df=7, **P
1066 =0.008).

1067 **E**, Effect of optogenetic excitation in EYFP (N = 6) and ChR2 (N = 8) groups on flight during WN
1068 in the high-threat context (LED-on vs LED-off, Paired t-test, ChR2, t=1.077, df=7, P =0.31).

1069 **F**, Effect of optogenetic excitation in EYFP (N = 6) and ChR2 (N = 8) groups on freezing during
1070 WN in the low-threat context (LED-on vs LED-off, Paired t-test, ChR2, t=3.748, df=7, **P
1071 =0.007).

1072 **G**, Effect of optogenetic excitation in EYFP (N = 6) and ChR2 (N = 8) groups on flight score
1073 during WN in the low-threat context (LED-on vs LED-off, Paired t-test, ChR2, t=2.211, df=7, P
1074 =0.06).

1075 **H**, Example fibre placements over the CeA for the eNpHR groups (N = 9)
1076 **I**, Example fibre placements over the CeA for the ChR2 groups (N = 9)

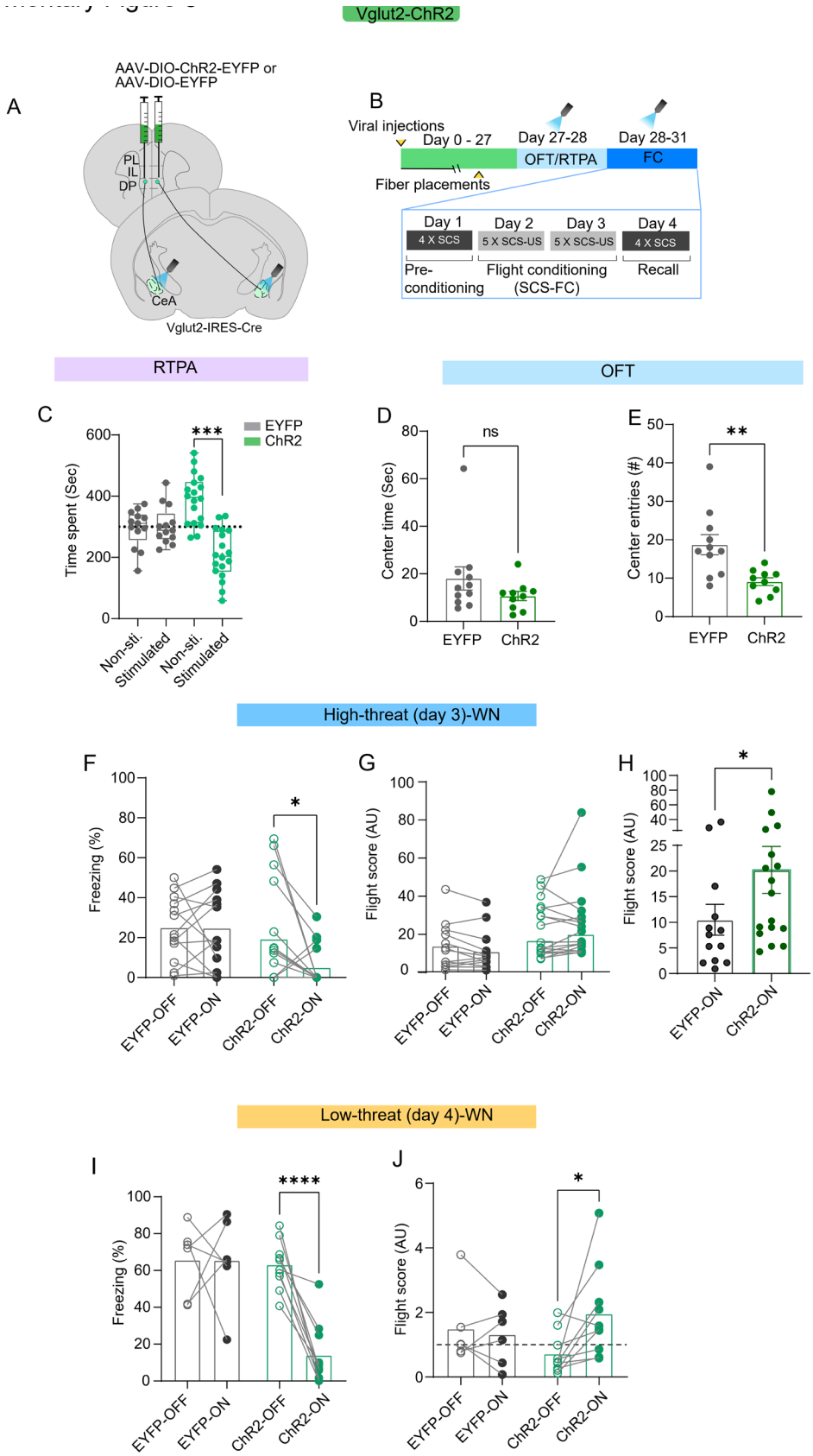
Vglut2-ChR2
A
AAV-DIO-ChR2-EYFP or
AAV-DIO-EYFP
PL
IL
DP
CeA
Vglut2-IRES-Cre
B
Viral injections
Day 0 - 27
Day 27-28
Day 28-31
OFT/RTPA
FC
Fiber placements
Day 1
Day 2
Day 3
Day 4
4 X SCS
5 X SCS-US
5 X SCS-US
4 X SCS
Pre-conditioning
Flight conditioning (SCS-FC)
Recall
RTPA
OFT
C
EYFP
ChR2
Time spent (Sec)
Non-sti.
Stimulated
Non-sti.
Stimulated
D
ns
Center time (Sec)
EYFP
ChR2
E
Center entries (#)
EYFP
ChR2
High-threat (day 3)-WN
F
Freezing (%)
EYFP-OFF
EYFP-ON
ChR2-OFF
ChR2-ON
G
Flight score (AU)
EYFP-OFF
EYFP-ON
ChR2-OFF
ChR2-ON
H
Flight score (AU)
EYFP-ON
ChR2-ON
Low-threat (day 4)-WN
I
Freezing (%)
EYFP-OFF
EYFP-ON
ChR2-OFF
ChR2-ON
J
Flight score (AU)
EYFP-OFF
EYFP-ON
ChR2-OFF
ChR2-ON

1077

1078 **Figure S8 (Data related figure 4): Effect of DP-CEA pathway stimulation in Vglut2 mice**

1079 **A,** Viral injection strategy for optogenetic terminal stimulation of DP-to-CeA neuronal projections

1080).

1081 **B**, Experimental timeline.

1082 **C**, Real-time place aversion (RTPA) performance of EYFP (N=13) and ChR2 (N=17) groups

1083 (paired t-test, EYFP (t=0.2167, df=12, P =0.83), ChR2 (t=4.713, df=17, ***P =0.0002).

1084 **D-E**, Effect of optogenetic excitation on OFT centre time (**D**) and number of entries into the

1085 centre zone (**E**) in EYFP (N=11) and ChR2 (N=10) groups (unpaired t-test (t=3.288, df=19, **P

1086 =0.01).

1087 **F**, Effect of optogenetic excitation in EYFP (N = 13) and ChR2 (N = 17) groups on freezing

1088 during WN in the high-threat context (LED-on vs LED-off, Paired t-test, ChR2, t=2.455, df=16,

1089 *P =0.025).

1090 **G**, Effect of optogenetic excitation in EYFP (N = 13) and ChR2 (N = 17) groups on flight during

1091 WN in the high-threat context (LED-on vs LED-off, paired t-test, ChR2, t=1.123, df=16).

1092 H, Comparison of flight scores in the LED-on condition between EYFP control and ChR2 groups

1093 (Mann Whitney test, **P* = 0.0433).

1094 **I**, Effect of optogenetic excitation in EYFP (N = 6) and ChR2 (N = 10) groups on freezing during

1095 WN in the low-threat context (LED-on vs LED-off, paired t-test, ChR2, t=7.135, df=9, ****P

1096 <0.0001).

1097 **J**, Effect of optogenetic excitation in EYFP (N = 6) and ChR2 (N = 10) groups on flight scores

1098 during WN in the low-threat context (LED-on vs LED-off, paired t-test, ChR2, t=t=2.717, df=9, *P

1099 = 0.02).

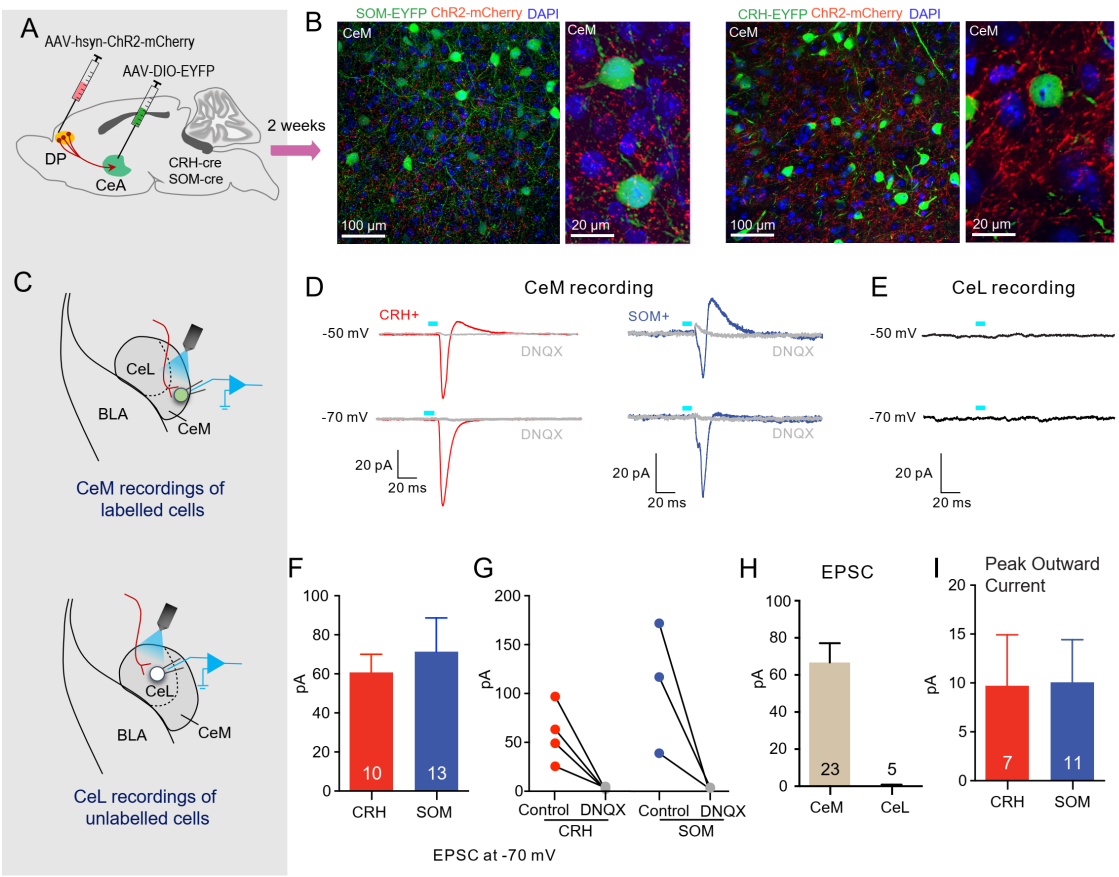

J **Firing Properties of DP-targeted CeA Neurons**

DP-Excited cells (n=11)				
Classification	**Spike Threshold** (mV)	**Spike Latency** (ms)	**Spike Frequency Adaptation** (3rd ISI/Last ISI)	**Sag** (% steady-state)
Regular spiking (n=5)	-42 ± 2	46 ± 12	0.62 ± 0.11	17 ± 1
Bursting (n=4)	-43 ± 2	80 ± 40	–	21 ± 7
Late-firing (n=2)	-45 ± 6	194 ± 46	0.62 ± 0.04	11 ± 2

Figure S9: Data related to Figure 5.

A, Schematic of targeting strategy for optogenetic stimulation.

B, DP terminals in CeM near SOM+ (*left*) and CRH+ (*right*) cells at 20x and 40x magnification.

C, Strategy for recording light-evoked synaptic input from DP to SOM+ or CRH+ neurons from CeM (*top*) and CeL (*bottom*) regions.

D, Representative evoked synaptic responses in CeM SOM+ and CRH+ cells by photostimulation of DP axonal fibres in voltage-clamp.

1108 **E**, Photostimulation of axonal fibres did not evoke responses in CeL neurons.

1109 **F**, Average amplitude of evoked EPSCs in CRH+ neurons (N = 10 cells from 3 mice) and SOM+

1110 (N = 13 cells from 3 mice) at -70mV. Unpaired Student's t-test, *p* = 0.63.

1111 **G**, Amplitudes of evoked EPSCs in CRH+ (N = 4 cells from 3 mice) and SOM+ (N = 3 cells from

1112 2 mice) neurons at -70 mV, before and after application of DNQX.

1113 **H**, Average amplitude of evoked EPSCs in CeM (N = 23 cells from 6 mice) and CeL neurons (N

1114 = 5 cells from 2 mice).

1115 **I**, The amplitude of disynaptic IPSCs evoked by ChR2 stimulation of DP terminals (Unpaired

1116 Student's t-test, $t_{(16)}$= 0.055; p = 0.96).

1117 **J,** The firing properties of DP-targeted CeM neurons.